Version of Record: https://www.sciencedirect.com/science/article/pii/S0005272824000173
Manuscript_4036a045ef2097c2879012f2b94aeed3

Two Pathways to Understanding Electron Transfer in Reaction Centers from Photosynthetic Bacteria: A Comparison of *Rhodobacter sphaeroides* and *Rhodobacter capsulatus* Mutants

Kaitlyn M. Faries[1], Deborah K. Hanson[2], James, C. Buhrmaster[2], Stephen Hippleheuser[2], Gregory A. Tira[2], Ryan M. Wyllie[2], Claire E. Kohout[2], Nikki Cecil M. Magdaong[1], Dewey Holten[1], Philip D. Laible[2], and Christine Kirmaier[1]*

[1]Department of Chemistry, Washington University, St. Louis, MO 63130

[2]Biosciences Division, Argonne National Laboratory, Lemont, IL 60439

* **Email:** Kirmaier@wustl.edu

Keywords

Charge Separation, Mutagenesis, Ultrafast Spectroscopy, Picosecond Kinetics

© 2024 published by Elsevier. This manuscript is made available under the Elsevier user license
https://www.elsevier.com/open-access/userlicense/1.0/

ABSTRACT

The rates, yields, mechanisms and directionality of electron transfer (ET) are explored in twelve pairs of *Rhodobacter (R.) sphaeroides* and *R. capsulatus* mutant RCs designed to defeat ET from the excited primary donor (P*) to the A-side cofactors and re-direct ET to the normally inactive mirror-image B-side cofactors. In general, the *R. sphaeroides* variants have larger $P^+H_B^-$ yields (up to ~90%) than their *R. capsulatus* analogs (up to ~60%), where H_B is the B-side bacteriopheophytin. Substitution of Tyr for Phe at L-polypeptide position L181 near B_B primarily increases the contribution of fast $P^* \rightarrow P^+B_B^- \rightarrow P^+H_B^-$ two-step ET, where B_B is the "bridging" B-side bacteriochlorophyll. The second step (~6–8 ps) is slower than the first (~3–4) ps, unlike A-side two-step ET ($P^* \rightarrow P^+B_A^- \rightarrow P^+H_A^-$) where the second step (~1 ps) is faster than the first (~3–4 ps) in the native RC. Substitutions near H_B, at L185 (Leu, Trp or Arg) and at M-polypeptide site M133/131 (Thr, Val or Glu), strongly affect the contribution of slower (20–50 ps) $P^* \rightarrow P^+H_B^-$ one-step superexchange ET. Both ET mechanisms are effective in directing electrons "the wrong way" to H_B and both compete with internal conversion of P* to the ground state (~200 ps) and ET to the A-side cofactors. Collectively, the work demonstrates cooperative amino-acid control of rates, yields and mechanisms of ET in bacterial RCs and how A- vs. B-side charge separation can be tuned in both species.

Graphical Abstract

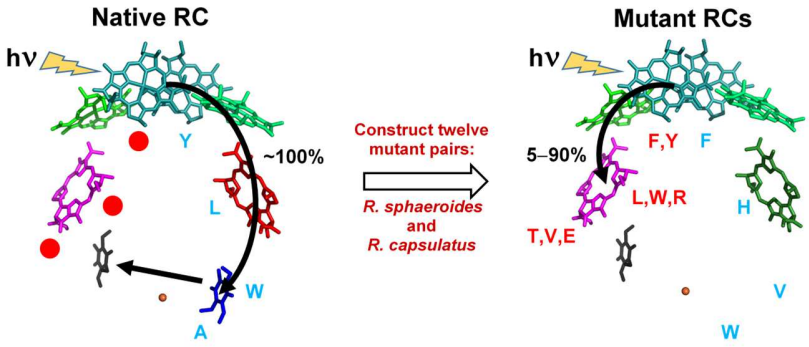

INTRODUCTION

The protein scaffolding in the reaction center (RC) from purple photosynthetic bacteria houses six bacteriochlorin and two quinone cofactors, tunes their electronic properties and controls the rates, yields and directionality of the charge-separation processes. The L and M polypeptides both have five transmembrane helices while the H polypeptide primarily resides on the cytoplasmic face of the RC (Figure 1A) [1-4]. The helices of the L and M polypeptides and bound cofactors have a pseudo C_2-symmetric arrangement. Light absorption generates the lowest singlet excited state (P*) of a bacteriochlorophyll (BChl) dimer (P). The dimer is flanked by monomeric BChls B_A and B_B adjacent to the Mg-free bacteriopheophytin (BPh) analogs H_A and H_B, followed by quinones Q_A and Q_B, bridged by a non-heme Fe^{2+}. Although structurally symmetric, the RC is functionally asymmetric (Figure 1B). Electron transfer (ET) from P* in the wild-type (WT) RC proceeds only via the A-side cofactors B_A and H_A to give $P^+Q_A^-$ in ~200 ps with essentially unity yield. ET from Q_A to Q_B occurs on the microsecond time scale. Following reduction of P^+ by a cytochrome, another round of A-side charge separation delivers a second electron to Q_B. These ET steps are coupled with the uptake of two protons to produce quinol Q_BH_2, which then leaves the RC. B-side cofactors B_B and H_B are non-participatory in the native RC.

Early transient-absorption (TA) studies revealed "wrong way" ET in the *R. capsulatus* "DH" mutant [8]. The "H" mutation (Figure 1C and Table 1) substitutes His for Leu at M212, centered over one face of H_A and results in replacement of H_A with a BChl (β_A) [8,9]. All mutants studied herein bear this mutation. This leaves a spectral window to assay the reduction of H_B. Additionally, since BChl is harder to reduce than BPh *in vitro* by 150–300 meV [13,14], $P^+\beta_A^-$ is much higher in free energy in the mutants than $P^+H_A^-$ in the native RC. The "D" mutation Gly → Asp at M201 near B_A destabilizes $P^+B_A^-$ [8]. The DH RC has a $P^+H_B^-$ yield of ~15% and a time

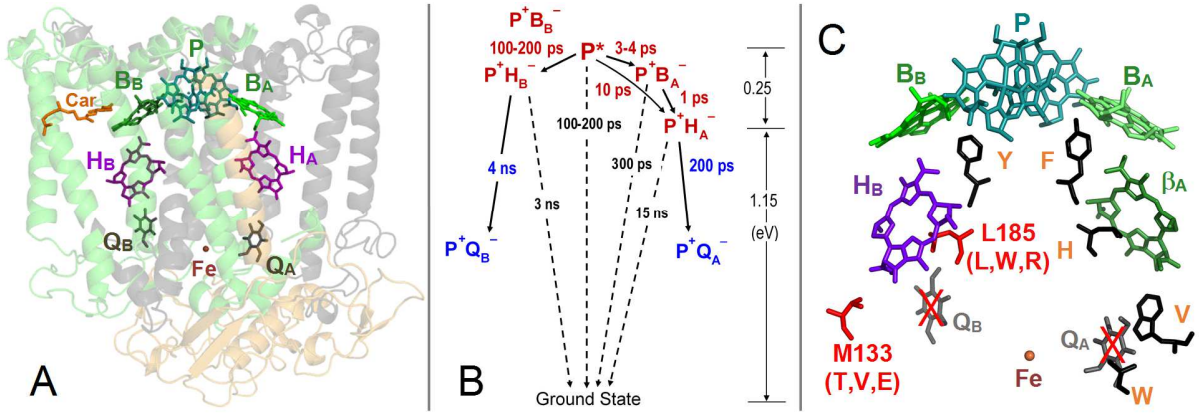

Figure 1. (A) Structure of the *R. sphaeroides* RC (1pcr) with polypeptides L (gray), M (green) and H (tan) and embedded cofactors: bacteriochlorophylls (green), bacteriopheophytins (purple), quinones (gray), carotenoid (orange) and non-heme Fe (brown). One helix of the M polypeptide traverses the transmembrane complex near the A-side cofactors and one helix of the L polypeptide traverses the complex near the B-side cofactors. (B) Model free energy diagram and time constants for forward ET (solid black) and charge recombination and P* internal conversion to the ground state (dashed black). (C) Sites for mutations in RCs in which BChl β_A replaces H_A. The native amino acids (black) are replaced by residues given by the single letter codes (orange or red) and are defined in Table 1. The native residue at L185 (red) is Leu in *R. sphaeroides* and Trp in *R. capsulatus*. The native residue at M133 (red) is Thr in *R. sphaeroides* and Val at the analogous M131 in *R. capsulatus*.

Table 1. Mutations and their utility.[a]

Individual Background Mutations					
R. sphaeroides		***R. capsulatus***			
Site	**Mutation**	**Site**	**Mutation**	**Code**	**Purpose**
L181	F → Y	L181	F → Y	Y	Stabilize $P^+B_B^{-b}$
M210	Y → F	M208	Y → F	F	Destabilize $P^+B_A^{-b}$
M214	L → H	M212	L → H	H	Replace H_A with BChl (β_A)[c]
M252	W → V	M250	W → V	V	Eliminate Q_A activity[d]
M260	A → W	M258	A → W	W	Eliminate Q_A activity[d]
Individual Additional Mutations					
L185	L → W	L185	W → L	W/L	Alter rates of $P^* \rightarrow P^+H_B^- \rightarrow P^+Q_B^-$
L185	L → R	L185	W → R	R	Alter rates of $P^* \rightarrow P^+H_B^- \rightarrow P^+Q_B^-$
M133	T → E	M131	V → E	E	Add H-bond to H_B and stabilize $P^+H_B^{-e}$
M133	T → V	M131	V → T	V/T	Alter the free energy of $P^+H_B^-$

[a] The residue numbers for the M polypeptide in *R. sphaeroides* are two larger than for the "equivalent" residue in *R. capsulatus* due to the presence of two additional amino acids near the beginning of the M polypeptide of *R. sphaeroides.* The L-polypeptides are identical length for the two species. [b]Calculations [5-7] indicate that Tyr M210/M208 stabilizes $P^+B_A^-$ by ~200 meV whereas PheL181 does not provide such stabilization of $P^+B_B^-$. [c]The pigment substitution [8-12] spectrally isolates the Q_x band of H_B and makes spectral analysis of $P^+H_B^-$ unambiguous. $P^+\beta_A^-$ is expected to lie higher in free energy than $P^+H_A^-$ by 150–300 meV based on the difference in reduction potentials of BChl *a* and BPh *a in vitro* [13,14]. [d]The W(M250/M252)V [15] and A(M258/M260)W [16] mutations weaken binding of Q_A resulting in its displacement or absence. Q_A is absent in the W(M252)V *R. sphaeroides* x-ray crystal structure (PDB Code 7mha) [17]. [e]A hydrogen bond between GluM133/M131 and the ring V keto group of H_B is indicated by the red shift of the Q_x band of H_B from 528 to 535 nm [18]. This hydrogen bond should stabilize $P^+H_B^-$ by 50–100 meV based on the effects of hydrogen bonds to BChl *a* and BPh *a* [19,20].

constant of ~100 ps for P* → $P^+H_B^-$ (Figure 1B). The yield of $P^+H_B^-$ increases to ~25% in the *R. capsulatus* YFH mutant [21]. In the YFH RC, TyrM208 near P and B_A is replaced with Phe ("F" in Figure 1C and Table 1) and symmetry-related PheL181 near P and B_B is replaced with Tyr ("Y" in Figure 1C and Table 1) to respectively raise $P^+B_A^-$ and lower $P^+B_B^-$ in free energy [5-7]. The P* decay in these mutants mainly produces $P^+\beta_A^-$ along with a small amount of P* internal conversion to the ground state with a derived time constant of ~100 ps for RCs in the detergent LDAO [21,22]. This value matches that obtained for the *R. capsulatus* D_{LL} mutant RC in LDAO, where P* decays solely to the ground state [23,24]. For the D_{LL} RC in Deriphat 160 C, internal conversion is ~180 ps [23,24], which is similar to the value observed in membranes [25,26]. These studies concur on a ~100–200 ps time constant for P* → ground state (Figure 1B).

The difference in free energy of $P^+B_A^-$ and $P^+B_B^-$ in the WT RC is thought to be key to unidirectional charge separation (Figure 1B) [5-8,21,27-32]. Current consensus places $P^+B_A^-$ ~70 meV below P* and $P^+B_B^-$ ~100 meV above P* [5-7,28-41]. This difference is due largely to the TyrM210/208 near B_A vs. PheL181 near B_B [5-7]. Thus, in the native RC, A-side ET occurs primarily by a two-step process P* → $P^+B_A^-$ → $P^+H_A^-$ (with τ_1 ~ 3–4 ps and τ_2 ~ 1 ps), whereas ET to the B side occurs by slower (100–200 ps) one-step superexchange in which $P^+B_B^-$ does not form but is the electronic mixing element between P* and $P^+H_B^-$ (Figure 1B).

A further distinction between the A- and B-side states is that $P^+H_A^-$ lies ~250 mV below P* [6,7,34,35,42] whereas $P^+H_B^-$ lies only ~70 meV below P* [37,43,44]. Delayed-fluorescence and transient-absorption studies (on RCs in which Q_A is removed or reduced to Q_A^-) indicate that as initially-formed $P^+H_A^-$ is closer to P* and is stabilized as a function of time by protein relaxations [42,45-50]. The substantial difference in free energies of $P^+H_B^-$ and $P^+H_A^-$ is due in part to a hydrogen bond between GluL104 and the ring V keto group of H_A [5,7,28]. Substitution

of Leu for GluL104 results in a blue shift of the H_A spectral features but does not change the ~100% yield of $P^+H_A^-$ for both *R. capsulatus* [51] and *R. sphaeroides* [52]. The symmetry-related residue near H_B is ThrM133 in *R. sphaeroides* and ValM131 in *R. capsulatus*. Incorporation of Glu at M133/131 ("E" in Figure 1C and Table 1) appears to add a hydrogen bond to the ring V keto group of H_B (as evidenced by a red shift of the H_B spectral features) and results in an increase in $P^+H_B^-$ yield [18,53-56]. The effect on the $P^+H_B^-$ yield depends on species and other mutations present, as further explored herein.

Residue L185 near H_B, symmetry related to M214/212 near H_A (Figure 1C and Table 1), is another focus of the work herein. Recently, we replaced LeuL185 in *R. sphaeroides* with all possible natural amino acids with the E-YFH "background" (Figure 1C and Table 1) [10]. Arg at L185 with E-YFH gives an ~90% yield of $P^+H_B^-$ [27,56]. Trp at L185 has a small effect with E-YFH but a substantially larger effect with YFH (lacking GluM133) [10,27]. There is clearly an interplay between stabilization of $P^+H_B^-$ by Glu at M133 and Trp or Arg at L185. Furthering this line of insight, the native residue at L185 is Trp for *R. capsulatus* compared to Leu for *R. sphaeroides*. Furthermore, the YFH substitutions (Figure 1C and Table 1) in *R. capsulatus* give a higher yield of $P^+H_B^-$ (~25%) than in *R. sphaeroides* (~15%) [18,21,22].

One focus here is whether this difference might derive from the native Trp in *R. capsulatus* vs. Leu in *R. sphaeroides* at L185. More generally, here ET is compared in twelve pairs of multiply-mutated RCs from these two species of photosynthetic bacteria. The pairs include all combinations of Leu or Trp at L185 and Thr, Val or Glu at M133/131 in the YFH background for both species. Collectively, the studies give new, comparative, systematic insight into amino-acid control of the rates, yields and directionality of charge separation in *R. sphaeroides* and *R. capsulatus* RCs.

II. MATERIALS AND METHODS

2.1 Mutants

Twelve pairs of *R. sphaeroides*/*capsulatus* RCs were constructed in which the residue at L185 is Leu, Trp or Arg and the residue at M133/131 is Thr, Val or Glu in conjunction with "background mutations" at other sites. The mutations are shown in Figure 1C and identified in Table 1 along with a brief description of their utility, which includes eliminating Q_A and Q_B activity. The new mutants are the *R. sphaeroides* **5S**, **7S**, **8S** and **9S** and *R. capsulatus* **4C**, **6C**, **7C**, **8C**, **10C** and **12C** (Table 2). For the other mutants, only the $P^+H_B^-$ yields have been reported previously. For all the mutants, the TA data encompassing the visible and near-infrared (NIR) and 100 fs to 100 μs were systematically analyzed and compared.

2.2. Mutant RC Preparation

The genetic systems developed for manipulation of *puf* operon genes of *R. capsulatus* [57] and *R. sphaeroides* [18] have been described previously, as have the methods for protein engineering, cell growth and RC purification [10]. All cultures for RC expression were grown chemoheterotrophically in 2 L of GYCC [18,58] medium (in a 2.8 L baffled Fernbach flask with a silicone sponge closure, 125 rpm, 33 °C, in the dark). Histidine-tagged mutant RCs were solubilized with Deriphat 160 C, purified via affinity chromatography and concentrated [18]. Ground-state absorption spectroscopy provided preliminary assessments of the effects of the genetic substitutions on expression yields and RC quality, stability and pigment content.

2.3. Spectroscopy

Transient absorption (TA) measurements spanning the visible (425–785 nm) and near-infrared (815–1350 nm) regions employed 100-fs 850-nm excitation flashes from a 1-KHz laser system (Spectra Physics) and Helios or EOS spectrometers (Ultrafast Systems) providing time delays to ~8 ns or ~0.5 ms, respectively. Studies utilized ~20 μM RCs in 10 mM Tris, 0.1% Deriphat 160 C, pH 7.8 to which sodium ascorbate in buffer and terbutryn in ethanol were added to give 100× and 25× concentrations, respectively, relative to the RCs. Samples were stirred using a magnetic stir bar in 2 mm quartz cuvettes. The data were analyzed using Surface XPlorer (Ultrafast Systems), CarpetView (Light Conversion) and custom routines in OriginPro (OriginLabs) [10]. The P/P^+ oxidation potentials vs. NHE were measured as described previously [33,56] for RCs in the same buffer used for TA studies. The $P^+H_B^-$ yields were determined as described previously [27]. In short, the integrated bleaching of the H_B $Q_x(0,0)$ and $Q_x(1,0)$ bands (~535 and ~500 nm, respectively) at 250 ps is compared to the integrated bleaching of the Q_x band of P (600 nm) at 0.4 ps. That ratio is compared to that for WT, where a 100% $P^+H_A^-$ yield is assumed.

III. RESULTS

3.1. Primary Photochemistry – Results Summary

Table 2 identifies the twelve *R. sphaeroides/capsulatus* mutant pairs, the residues present at M133/131 and L185, and the background (WT, H, FH or YFH as defined in Figure 1C and Table 1). Mutant pairs 1–3 have the native residues at M133/131 and L185. The other nine pairs utilize the FH background (pairs 4 and 5) or YFH background (pairs 6–12) and compare Thr, Val or Glu at M133/131 and Trp, Leu or Arg at L185 in the two species.

Table 2. P* decay-product yields and decay-profile parameters.

Pair #	X[a]	M133 or M131[b]	L185[c]	Name[d]	P/P$^+$ (mV)[e]	P$^+$H$_B^-$ yield (%)[f]	GS Yield (%)[g]	P$^+\beta_A^-$ yield (%)[h]	τ_1 (ps)[i]	A_1 (%)[i]	τ_2 (ps)[i]	A_2 (%)[i]	τ_3 (ps)[i]	A_3 (%)[i]	τ_{AWA2} (ps)[j]	τ_{AWA3} (ps)[k]	τ_{P+HB-} (ns)[l]
Native at M133/131 and L185																	
1	S	*Thr*	*Leu*	WT^V	491	≤2[m]	≤2[m]	≥96[m]	2.4	70	9	30	-	-	4	-	19
	C	*Val*	*Trp*	WT^V	489	≤2[m]	≤2[m]	≥96[m]	3.1	70	21	30	-	-	8	-	15
2	S	*Thr*	*Leu*	H	472	6	4	90	4.0	73	27	21	199	6	9	21	5.6
	C	*Val*	*Trp*	H	477	6	9	85	3.5	48	20	30	132	22	10	37	5.8
3	S	*Thr*	*Leu*	FH	499	7	52	41	3.8	19	42	39	240	42	30	119	5.1
	C	*Val*	*Trp*	FH	501	7	62	31	4.7	11	72	33	251	56	56	166	7.6
Glu at M133/131 and Leu vs. Trp at L185 in FH background																	
4	S	Glu	*Leu*	E-FH	506	46	35	19	4.5	15	37	46	139	39	29	71	9.0
	C	Glu	Leu	EL-FH	486	20	51	29	4.5	12	57	39	234	49	45	137	6.5
5	S	Glu	Trp	EW-FH	488	46	46	8	4.4	12	49	41	141	47	39	87	11
	C	Glu	*Trp*	E-FH	492	20	56	24	3.2	10	71	41	220	49	57	138	9.3
Thr vs. Val at M133/M131 and Leu vs. Trp at L185 in YFH background																	
6	S	*Thr*	*Leu*	YFH	472	14	14	72	3.9	43	20	37	163	20	11	41	4.2
	C	Thr	Leu	TL-YFH	477	4	28	68	4.5	32	31	32	219	36	18	89	5.8
7	S	*Thr*	Trp	W-YFH	472	52	11	37	3.9	33	18	44	73	23	12	26	4.0
	C	Thr	*Trp*	T-YFH	470	13	23	64	4.6	33	38	39	222	28	23	79	5.0
8	S	Val	*Leu*	V-YFH	472	32	5	63	3.9	45	19	40	133	16	11	30	3.7
	C	*Val*	Leu	L-YFH	480	12	22	66	3.8	26	27	38	188	36	17	79	7.6
9	S	Val	Trp	VW-YFH	473	68	17	15	3.5	32	18	47	79	21	12	26	13
	C	*Val*	*Trp*	YFH	474	23	24	53	3.3	28	28	41	147	31	18	58	8.9
Glu at M133/131 and Leu vs. Trp vs. Arg at L185 in YFH background																	
10	S	Glu	*Leu*	E-YFH	473	72	9	19	4.0	43	18	44	80	13	11	20	7.4
	C	Glu	Leu	EL-YFH	478	33	12	55	5.0	32	26	44	149	24	17	49	7.2
11	S	Glu	Trp	EW-YFH	472	70	17	13	4.0	35	21	48	74	17	14	24	14
	C	Glu	*Trp*	E-YFH	467	45	23	32	4.0	26	32	49	125	25	22	48	8.9
12[n]	S	Glu	Arg	ER-YFH	495	91	4	5	4.0	40	22	50	150	10	14	27	17
	C	Glu	Arg	ER-YFH	486	53	23	24	4.5	27	29	42	156	31	19	61	12

[a]Species *R. sphaeroides* (S) or *R. capsulatus* (C).

[b]Residue present at M133/M131. The native residue is indicated by italics: *Thr* (*R. sphaeroides*) or *Val* (*R. capsulatus*).

[c]Residue present at L185. The native residue is indicated by italics: *Leu* (*R. sphaeroides*) or *Trp* (*R. capsulatus*).

[d]The mutant name has the form X-Z, where X refers to substitutions made at M133/M131 and L185, and Z refers to substitutions at L181, M210/208 and M214/212 using the abbreviations defined in Figure 1C and Table 1. *Not listed are the "V" or "VW" mutations, which are always present to inhibit Q_A activity/binding* [15-17].

[e]Measured P oxidation potential (typically ±3 mV) versus NHE for RCs in Tris/Deriphat.

[f]Yield of P$^+$H$_B^-$ from integrated Q_X bleaching referenced to 100% P$^+$H$_A^-$ for WT^V or WT^{VW} (± 7% of the measured value).

[g]Yield of P* internal conversion to the ground state.

[h]Yield of P$^+\beta_A^-$ for all RCs except WT^V (or WT^{VW}), for which the yield is that of P$^+$H$_A^-$.

[i]Parameters for P*stimulated emission decay (~920 nm).

[j]Amplitude-weighted-average lifetime from P* decay components 1 and 2.

[k]Amplitude-weighted-average lifetime from P* decay components 1, 2 and 3.

[l]Mean time constant for P$^+$H$_B^-$ decay.

[m]A 100% yield of P$^+$H$_A^-$ for WT^V and WT^{VW} is the reference value for the yield of P$^+$H$_B^-$ in the mutants. The yields of P* decay to produce P$^+$H$_B^-$ and P* decay to the ground state are both estimated to be ~2% for WT^V and WT^{VW} [27].

[n]The cultures from which RCs were obtained have comparable Klett values (culture density; 230 for mutant **12S** and ~249 for mutant **12C**) [27]. See Figure S11 and Table S2 for additional results.

Figure 2 (*R. sphaeroides*) and Figure 3 (*R. capsulatus*) provide "logic circuits" showing a "pathway" relating the mutant RCs for both species. The panel for each mutant gives the native (black) or substituted (blue) amino acids near the cofactors. The arrows indicate the single amino-acid substitution made at each "step". For *R. sphaeroides* (Figure 2), the first three mutants in the middle row hold constant the native LeuL185 while M133 is Val, Thr (native) or Glu. The first three mutants in the bottom row in Figure 2 substitutes Trp at L185 in conjunction with the same three M133 substitutions. Similarly, for *R. capsulatus* (Figure 3), the first three mutants in the middle row employ the native TrpL185 with M131 as Thr, Val (native) or Glu, and the first three mutants in the bottom row substitutes Leu at L185 with the same variations of residues at M131. The measured yields (Table 2) of the three products of P* decay – ET to the B side, internal conversion to the ground state, and ET to the A side – are given immediately below the pigment diagrams in each panel in Figures 2 and 3. Each panel also has a state diagram indicating the expected results of a mutation (*e.g.,* formation of a hydrogen bond) on free energy of the targeted state (see Table 1 footnotes). These are qualitatively consistent with the observed effect of the mutation on the $P^+H_B^-$ yield.

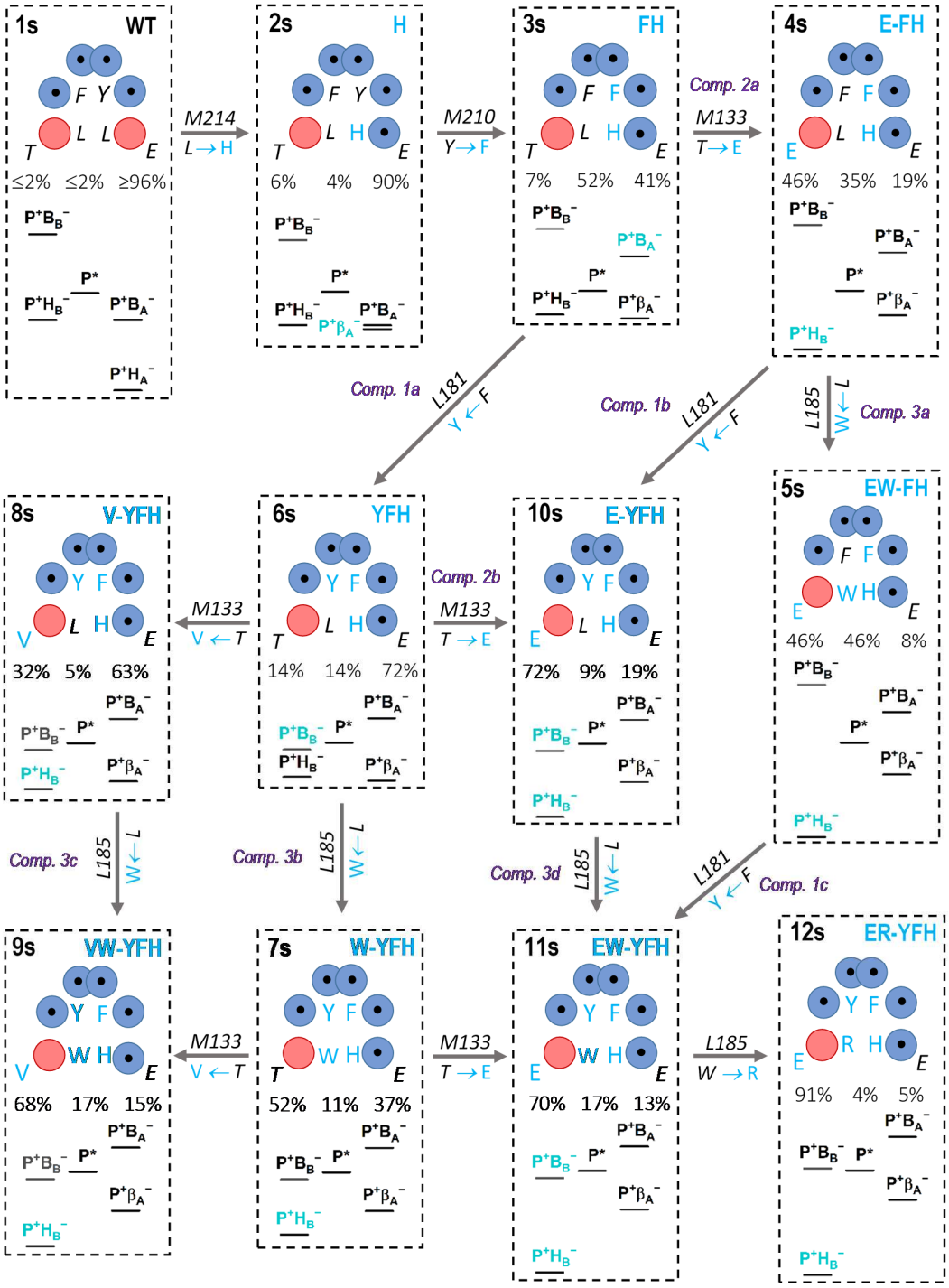

Figure 2. *R. sphaeroides* RC single-site "mutation circuit diagram." Each arrow indicates a single amino acid change. Native amino acids are in black italics and mutations in blue regular font. In each row, the free energies of the P* states are aligned. The charge-separated states are placed in free energy relative to P* in an illustrative manner, using literature values for effects of mutations (Table 1) and the measured P/P^+ potentials (Table 2); the relative free energies are qualitatively consistent with the measured yields (middle set of percentages, left to right) $P^+H_B^-$, P*→ ground state, and $P^+\beta_A^-$/ $P^+H_A^-$. Cyan font in a state diagram indicates the state(s) targeted to change in free energy compared to the precursor RC due to the mutation (arrow). See text for further details.

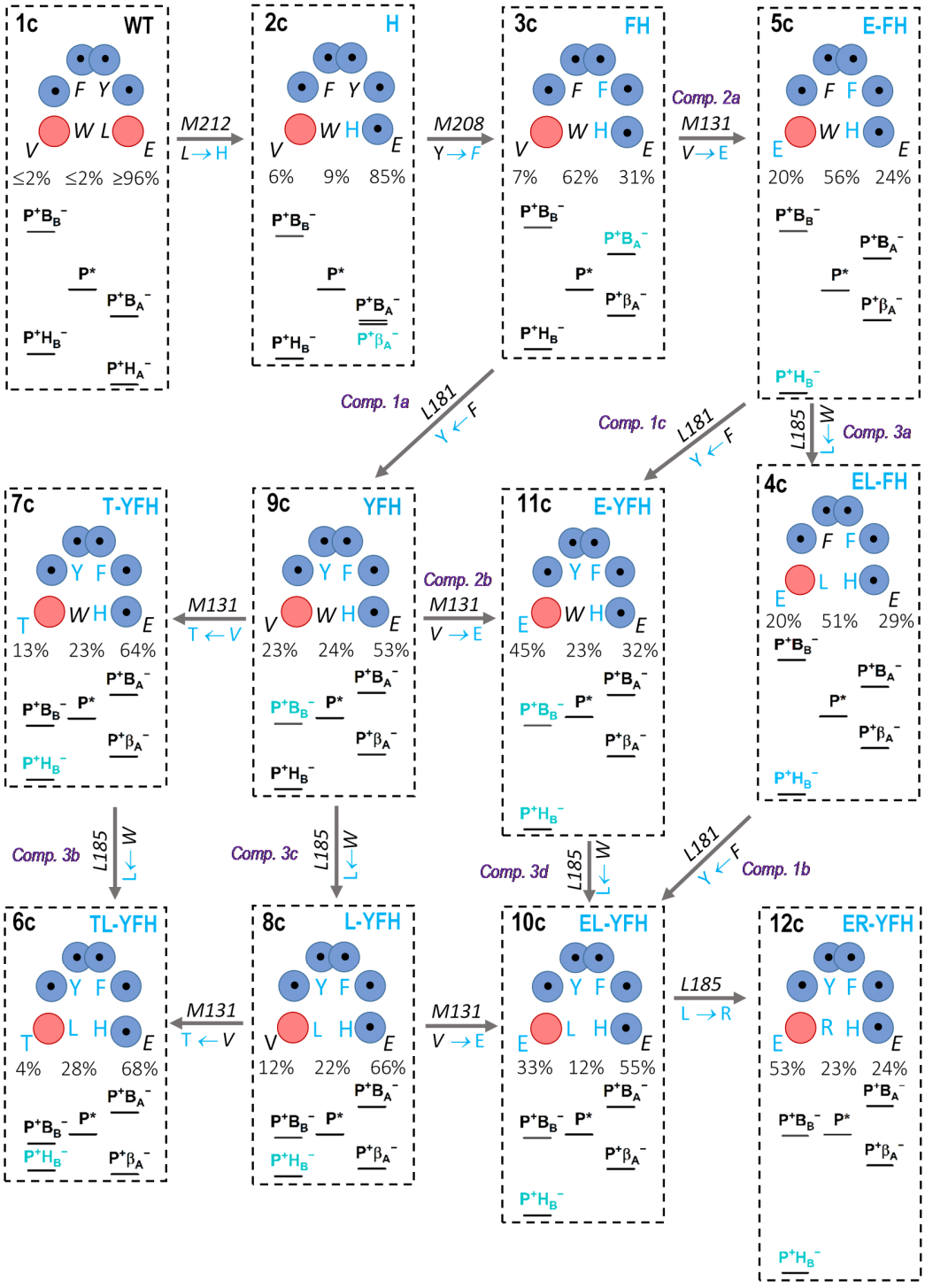

Figure 3. *R. capsulatus* RC single-site "mutation circuit diagram." Each arrow indicates a single amino acid change. Native amino acids are in black italics and mutations in blue regular font. In each row, the free energies of the P* states are aligned. The charge-separated states are placed in free energy relative to P* in an illustrative manner, using literature values for effects of mutations (Table 1) and the measured P/P$^+$ potentials (Table 2); the relative free energies are qualitatively consistent with the measured yields (middle set of percentages, left to right) $P^+H_B^-$, P*→ ground state, and $P^+\beta_A^-$/ $P^+H_A^-$. Cyan font in a state diagram indicates the state(s) targeted to change in free energy compared to the precursor RC due to the mutation (arrow). See text for further details.

3.2. TA Difference Spectra vs Time for Mutant Pair 11 as an Example

Visible and NIR TA difference spectra for *R. sphaeroides/capsulatus* mutant pair 11 are shown in Figure 4. These RCs have GluM133/131 and TrpL185 near H_B in the YFH background (Figures 2 and 3). The native residues are ThrM133 and LeuL185 (*R. sphaeroides*) and ValM131 and TrpL185 (*R. capsulatus*). Hence, the mutant names are EW-YFH (*R. sphaeroides*) and E-YFH (*R. capsulatus*) and are denoted **11S** and **11C**, respectively (Table 2). The spectra in Figure 4 for mutants **11S** (solid) and **11C** (dashed) are normalized to the same initial P* concentration. Thus, relative amplitudes of the spectral features reflect the relative amounts of states present.

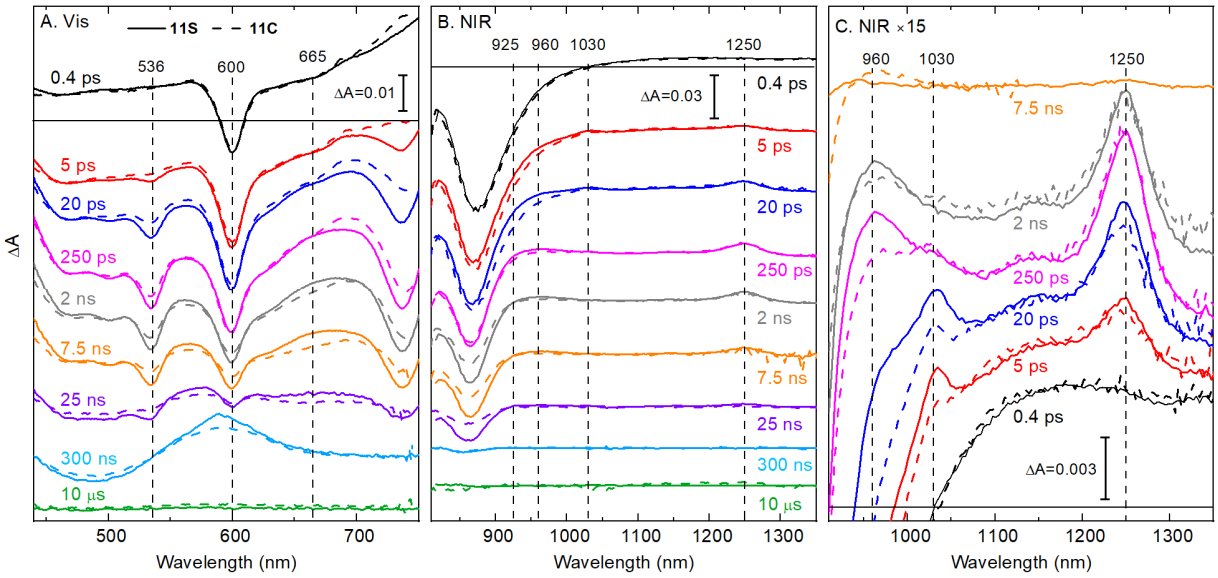

Figure 4. Ultrafast TA difference spectra in the visible (A) and NIR (B) regions at select times after excitation for (**11S**, solid) and (**11C**, dashed) RCs. Panel C focuses on region >920 nm using a ×15 vertical scale versus panel B and a reversed top-to-bottom order of the spectra but using the same color coding. The horizontal line in each panel is the ΔA = 0 line for the spectrum at 0.4 ps.

For both species, the spectrum at 0.4 ps (black) shows bleaching of the Q_x (600 nm) and Q_y (865 nm) bands of P and featureless excited-state absorption of P*. Stimulated emission from P* (maximum ~925 nm) partly overlaps the Q_y bleaching of P to give the broad negative-going feature at 865 nm (Figure 4B, black). The P* stimulated emission has decreased between 0.4 ps and 5 ps (Figures 4B and 4C, red). A small bleaching of the $Q_x(0,0)$ band of H_B (536 nm), due to

some formation of $P^+H_B^-$, is evident at 5 ps but not at 0.4 ps. This bleaching is more prominent for **11S** vs. **11C** (Figure 4A, red solid vs. dashed). The NIR spectra at 5 ps also display a small BChl-anion feature at 1030 nm (Figure 4B and 4C, red). This could originate from $P^+B_B^-$, $P^+B_A^-$ and/or $P^+\beta_A^-$. The 1030-nm feature at 5 ps is larger for **11S** than **11C** (Figure 4C, red). The formation of $P^+B_B^-$, $P^+B_A^-$ and/or $P^+\beta_A^-$ between 0.4 and 5 ps is also indicated by an increase in the bleaching of the Q_x band at 600 nm (Figure 4A, red vs. black). The feature at 1250 nm is due to P^+ and reflects the total amount of charge-separated states present at any time (Figure 4C, red).

The spectra at 20 ps (Figure 4, blue) are similar to those at 5 ps, but reveal increases in both H_B Q_x bleaching (536 nm) and P^+ absorption (1250 nm) due to formation of more $P^+H_B^-$. At 250 ps, the P* stimulated emission (925 nm) is substantially decreased, and again the H_B Q_x bleaching (536 nm) and P^+ absorption (1250 nm) have increased (Figure 4, magenta). Additionally, a feature at ~960 nm attributable (Figure S6) [13,14]) to H_B^- is more prominent. The spectral changes between 20 ps and 250 ps indicate slow formation of $P^+H_B^-$, which doesn't reach its maximal amplitude until ~250 ps. Integration of the bleaching of the H_B Q_x bands at 250 ps (Materials and Methods) shows a larger $P^+H_B^-$ yield for **11S** (70%) than for **11C** (45%) (Table 2).

The 250 ps spectrum for *R. sphaeroides* mutant **11S** shows little BChl anion absorption at 1030 nm (Figure 4C, solid magenta). This is consistent with the low (~20%) yield of $P^+\beta_A^-$ for **11S**, and that ~70% of its initial amplitude would remain at 250 ps, because that state decays primarily with a time constant of ~1 ns [9-12]. This indicates that the 1030-nm BChl-anion feature observed at 5 ps and 20 ps for **11S** is not due to primarily to $P^+\beta_A$. Additionally, one expects (Table 1) that the Y(M210)F mutation in **11S**, and Y(M208)F in **10C**, should raise $P^+B_A^-$ above P* [5-7]. Furthermore, if $P^+B_A^-$ were to form, at least some of its decay should produce $P^+\beta_A^-$ by $P^* \rightarrow P^+B_A^- \rightarrow P^+\beta_A^-$ two-step ET. Collectively, these considerations indicate that the main

contribution to the BChl anion absorption at 5 ps and 20 ps (Figures 4B and 4C, red and blue) for **11S** is from the $P^+B_B^-$ intermediate in the two-step ET process $P^* \rightarrow P^+B_B^- \rightarrow P^+\beta_B^-$. This process likely also contributes for **11C** (but not as substantially because the 1030 nm band at 5 and 20 ps is smaller) along with some formation of $P^+\beta_A^-$ (indicated by the small 1030 nm band at 250 ps).

Moving from 250 ps to 2 ns to 7.5 ns to 25 ns (Figure 4, magenta to gray to orange to violet) reveals decay of $P^+H_B^-$. This is evidenced by progressive diminution of (1) the H_B bleach at ~535 nm, (2) the Q_x bleach of P at 600 nm, (3) the short-wavelength side of the Q_y bleach of P (830 nm), and (4) the H_B anion absorption at 960 nm. The $P^+H_B^-$ decay has a (mean) time constant of ~14 ns for **11S** and ~9 ns for **11C** (Table 2) and occurs by charge recombination to give the ground state, (after spin rephasing) the triplet excited-state of P (P^R), and thermal repopulation of $P^+B_B^-$ and/or P*.

At 25 ns, the features due to $P^+H_B^-$ are greatly diminished. In the visible region (Figure 4A, violet), the residual Q_x bleachings at 536 nm and 600 nm rest on a non-uniform baseline whose origin is revealed at 300 ns to be the negative (490 nm) and positive (590 nm) wings of a broad derivative-like feature (Figure 4A, light blue). The 300-ns spectrum has no bleach of the Q_y band of P (865 nm) (Figure 4B, light blue) and reflects Car^T, the triplet excited state of the carotenoid (Figure 1A). Car^T forms from P^R (by energy transfer) with τ ~ 30 ns for **11S** and τ ~ 100 ns for **11C**, and then decays with τ ~ 3.6 μs for **11S** and τ ~ 4.3 μs for **11C**, respectively (Table S1 of the Supplemental Information). The $\Delta A = 0$ baseline is reached by 10 μs across the visible and NIR for both species (Figure 4, green). Sections S2–S7 give TA data for all 24 mutants.

3.3. Single-Wavelength Time Profiles for Mutant Pair 11 as an Example

The TA data for **11S** and **11C** (Figure 4) and for all mutants (Supplemental Information) span over eight orders of magnitude from ~100 fs to >10 μs, reaching ΔA = 0 at all wavelengths. Global fits (see next section) to a time-wavelength data set requires seven or eight exponentials. Minimally three components with time constants of ~2–5 ps (P_1*), ~20–70 ps (P_2*) and ~100–250 ps (P_3*) are required for P* decay. At least one component is needed for decay of $P^+\beta_A^-$ (~1 ns), one or two components for $P^+H_B^-$ (~3–20 ns), one for P^R (~20–120 ns) and one for Car^T (3–5 μs). Fits to kinetic profiles at individual wavelengths may require fewer exponentials depending on which excited or charge-separated states contribute to those spectral changes. Multi-exponential fits at key wavelengths for mutants **11S** and **11C** are shown in Figure 5.

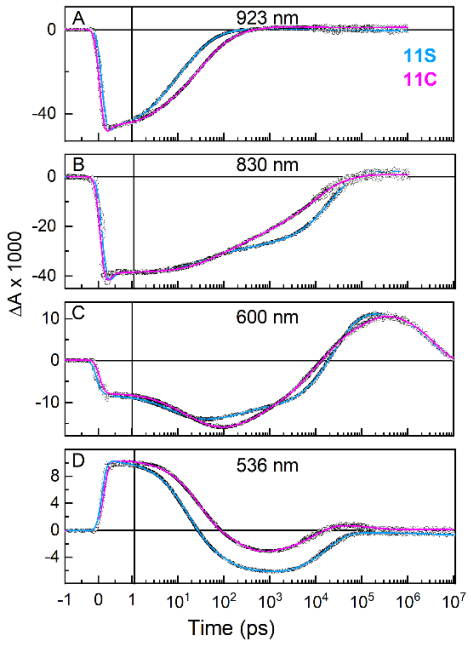

Figure 5. Kinetic profiles (open circles) and multi-exponential fits for mutants R. *sphaeroides* **11S** (blue lines) and *R. capsulatus* **11C** (magenta lines). A time axis is linear from –1 to 1 ps and logarithmic past 1 ps.

Decay of P* stimulated emission dominates at ~925 nm (Figure 5A) requires (minimally) three exponentials (Table 2). A fourth component of small amplitude, opposite sign, and longer time constant accounts for decay of $P^+H_B^-$ and other products (see Figure S3 for residuals). A

three-exponential fit is a convenient means to categorize what is likely a distribution of P* "populations" to facilitate comparisons among mutants. Figure 5A shows that the P* decay is faster for **11S** than **11C**, which is a common difference for RCs from *R. sphaeroides* vs. *R. capsulatus*.

Figure 5B shows time profiles at 830 nm, on the short-wavelength side of P Q_y bleaching where P* stimulated emission is minimal. Some return of RCs to the ground state occurs during P* decay (*i.e.,* <1 ns). In the range 1–100 ns (10^3–10^5 ps), compared to *R. sphaeroides* **11S** R. *capsulatus* **11C** shows a larger contribution of $P^+\beta_A^-$ decay, faster decay of $P^+H_B^-$ and slower decay of P^R, again typical differences between the two species. The fraction of the P bleaching that decays on the time scale ≥3 ns gives a second measure of the $P^+H_B^-$ yield and agrees well with that determined from integrated H_B Q_x bleaching at 250 ps.

Fitting the time evolution at 600 nm in Figure 5C for all mutants requires seven or eight exponentials to span the time scales that were probed (~100 fs >10 μs). All the excited and charge-separated states (involving P, B_B, β_A, B_A, Car) contribute substantially at ~600 nm via ground-state Q_x bleaching and/or transient absorption. Growth and decay of H_B Q_x bleaching contributes substantially to the time evolution at 536 nm in Figure 5D. The concentration $P^+H_B^-$ nearly maximizes by ~250 ps, increasing slightly at ~1 ns. The latter may be due to thermal repopulation of P* by charge-separated states such as $P^+\beta_A^-$, which then gives a small (<10%) additional amount of $P^+H_B^-$. Figure 5D shows that the amplitude of H_B bleaching (and $P^+H_B^-$ yield) is greater for **11S** than **11C**, another typical difference between the two species.

3.4. Global Analysis (DADS) for Mutant Pair 11 as an Example

The TA data sets in the visible and NIR regions were analyzed globally in a model-independent manner typically employing seven components (exponentials) to produce decay-associated difference spectra (DADS). Section S8 gives DADS for all 24 RCs. Analysis of the DADS for **11S** and **11C** (Figure 6) parallels that given above for the raw TA spectra and kinetics.

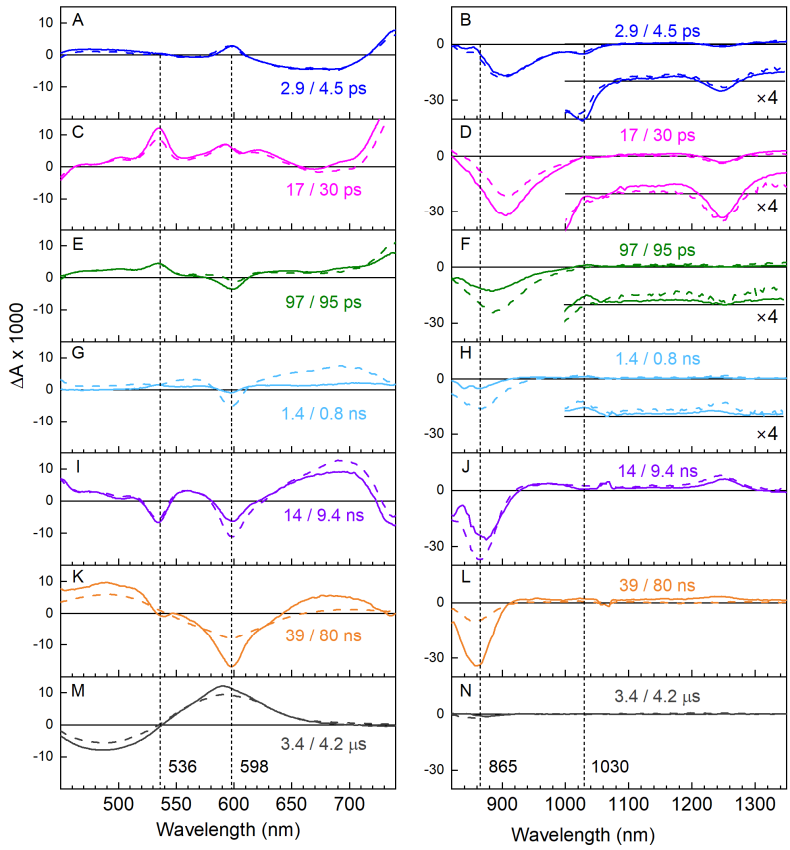

Figure 6. DADS in the visible (left) and NIR region for mutants **11S** (EW-YFH; solid) and **11C** (E-YFH; dashed) using seven components (exponentials). An eighth exponential ($\tau = 0.1$ ps) accounted for "flash artifacts" such as scattered excitation light. The DADS shown here employ the visible-NIR average time constant (from free fits) for each component. Basically the same DADS are obtained from free fits or using time constants for the three P* decay components fixed at values given in Table 2. The DADS largely reflect spectral changes due to P_1* (A,B), P_2* (C,D), P_3* (E,F), $P^+\beta_A^-$ (G,H), $P^+H_B^-$ (I,J), P^R (K,L), Car^T (M,N).

The ~3–5 ps (P_1*) DADS for **11S** and **11C** (Figures 6A and 6B) show decay of P* stimulated emission (~925 nm), growth of BChl Q_x bleaching (~600 nm) and growth of BChl-anion (*i.e.*, B_B^-) absorption (~1030 nm). Modelling of P* $\rightarrow$ $P^+B_B^-$ $\rightarrow$ $P^+H_B^-$ for **11S**, like **12S**

[27], reveals that the second step is slower (6–8 ps) than the first (~3 ps). Formation $P^+H_B^-$ is seen in the 17–30 ps (P_2*) DADS (Figures 6C and 6D). However, the amplitude of H_B Q_x bleach formation and growth in the 1250 nm band of P^+ in the ~17 ps DADS for **11S** cannot be accounted for by moving the electron from B_B to H_B or by the small amount of $P^+\beta_A^-$ produced. Thus, P* → $P^+H_B^-$ superexchange ET contributes significantly to the P_2* component for **11S** and **11C**, like other mutants studied here.

The ~100 ps DADS (Figures 6E and 6F) for **11S** and **11C** show characteristics of P* → $P^+H_B^-$ ET competing with P* → ground state. Both processes have an ~50% yield assuming the above-noted ~200 ps time constant for internal conversion. The features in the ~100 ps DADS include (1) decay of P* stimulated emission (~925 nm), (2) decay of P Q_y bleaching (~865 nm) and P/BChl Q_x bleaching (~600 nm), (3) growth of H_B Q_x bleaching (~536 nm), and (4) growth of P^+ (~1250 nm). A small decay of a BChl anion (1030 nm) may reflect a contribution of $P^+\beta_A^-$ → P* for **11S** based on analogy to mutants **2S** and **2C** (Figures S63 and S64) wherein the dominant ~1 ns decay $P^+\beta_B^-$ is accompanied by a small (~15%) ~200 ps component that might signal thermal repopulation of P* from an "unrelaxed" form of $P^+\beta_A^-$ [9,12]. This contribution is small for **11S** because of the low $P^+\beta_A^-$ yield and high $P^+H_B^-$ yield (Table 2).

The DADS in Figures 6I and 6J show differences between **11S** and **11C** in the decay of $P^+H_B^-$ (and formation of P^R and the ground state) that are relevant to trends among the mutants. In prior studies [10,27,55,56,59], the decay of $P^+H_B^-$ was fit with two exponentials with time constants of ~3 ns and ≥12 ns, and analyzed in analogy to the widely studied decay of $P^+H_A^-$ in WT RCs and A-side mutants wherein Q_A is depleted or reduced to Q_A^- [12,45-50,60,61]. The faster (*e.g,* unrelaxed) component involves in part thermal repopulation of $P^+B_B^-$ or P*. The slower (*e.g.,* relaxed) component reflects primarily two "parallel" decay routes (1) charge recombination

yielding the ground state (from singlet $P^+H_B^-$) and (2) spin-rephasing (to triplet $P^+H_B^-$) followed by charge recombination yielding P^R. Here, we report a single (mean) time constant for $P^+H_B^-$ decay (Table 2) because the short lifetime of P^R in *R. sphaeroides* (~20–30 ns) is similar to that of the longer-lived (relaxed) form of $P^+H_B^-$. Figure 6I shows that the mean decay of $P^+H_B^-$ for **11C** (9.4 ns) is shorter than that for **11S** (14 ns). Related to this (Table 2), the mean $P^+H_B^-$ decay time decreases in the order **11S** (EW-YFH; 14 ns) > **10S** (E-YFH; 7.4 ns) > **6S** (YFH; 4.2 ns), for example. Stabilization of $P^+H_B^-$ by TrpL185 or GluM133 or both reduces thermal repopulation of $P^+B_B^-$ or P* and increases the weighting of the (relaxed) forms of $P^+H_B^-$, lengthening the mean lifetime. Thus, stabilization of $P^+H_B^-$ by the mutations both increases the yield of the state and alters its decay characteristics in a consistent manner.

3.5. Comparison of Visible Region TA Spectra and $P^+H_B^-$ Yields for the 12 Mutant Pairs

Figure 7 shows the visible-region TA spectra at 250 ps from which $P^+H_B^-$ yields in Table 2 were obtained (Materials and Methods) [27,56]. Key points from Figure 7 are as follows. Addition of a hydrogen bond to H_B consistently shifts the $Q_x(0,0)$ band from ~528 to ~535 nm and the H_B anion band from ~620 to ~665 nm in RCs from both species. This substitution increases the yield of $P^+H_B^-$ (by stabilizing the state; Table 1), but typically by a larger factor for the *R. sphaeroides* vs. *R. capsulatus* mutant. For mutant pairs 4–12, each pair having the same residues at L185 and M133/131 in the same background, the $P^+H_B^-$ yield for the *R. sphaeroides* mutant RC is larger than that for the *R. capsulatus* analog (Figure 7 and Table 2).

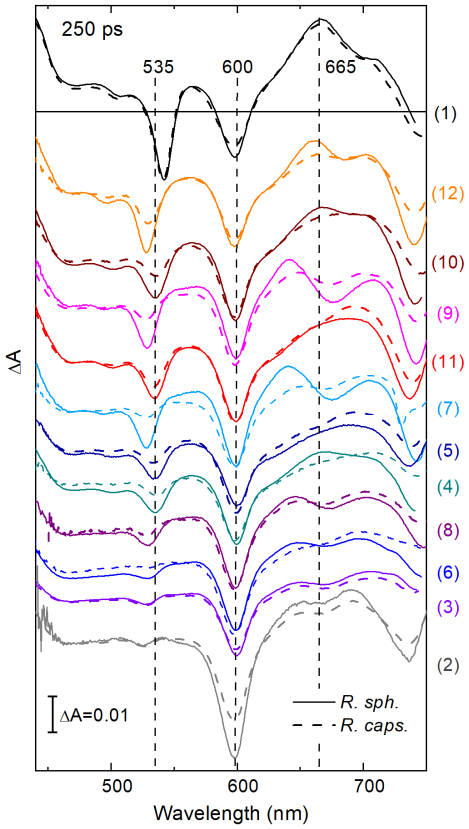

Figure 7. Ultrafast TA difference spectra in the visible region at 250 ps after excitation of RCs for 12 *R. sphaeroides* (solid) and *R. capsulatus* (dashed) mutant pairs, indicated by the number in parenthesis at the right (Table 2). The spectra are ordered vertically by decreasing $P^+H_B^-$ yield except for pair 1 (WT^V) which has ~100% $P^+H_A^-$ yield. The horizontal line reflects ΔA = 0 for pair 1. This line roughly bisects the ~600 nm P bleaching and the same applies to ΔA = 0 for the spectra for the other mutants. The vertical dashed lines are approximate positions of H_B Q_x bleach (~535 nm) P/BChl Q_x bleach (~600 nm) and H_B anion absorption.

3.6. Independent Assay of B-Side ET from NIR TA Spectra

Figure 8 shows TA data in the 910–1330 nm region at select times after excitation for each mutant. These data give an independent assessment of the relative amounts of P* and the A- and B-side charge-separated states present at a given time. Marked by the vertical dashed lines in Figure 8 are spectral positions assaying for the H_B anion (930–960 nm), BChl anions (1025 nm) and total P^+ (1245 nm). In each panel in Figure 8, the gray dotted line overlapping the 250-ps spectrum (red) is a *spectral fit* (820–1350 nm) employing the known basis spectra for $P^+H_B^-$, $P^+\beta_A^-$ and P* (Figure S7 and Section S2). At 250 ps, (1) $P^+H_B^-$ has basically reached its maximum

amplitude and has not decayed, (2) contributions from short-lived $P^+B_B^-$ (or $P^+B_A^-$) are minimal, and (3) $P^+\beta_A^-$ retains ~70% of its initial amplitude because it primarily decays with τ ~ 1 ns with a small (~15%) τ ~ 200 ps component (*vide supra*). The results of the spectral fits return a $P^+H_B^-$ yield for each mutant that agrees well with values from (1) decay of P bleach (830 nm) and (2) integrated H_B Q_x bleach at 250 ps, the latter being the prime assay (Figure S10). The yields of $P^+\beta_A^-$ and P* → ground state from NIR spectral simulations combine with those from P bleach decay to give the reported values (Table 2).

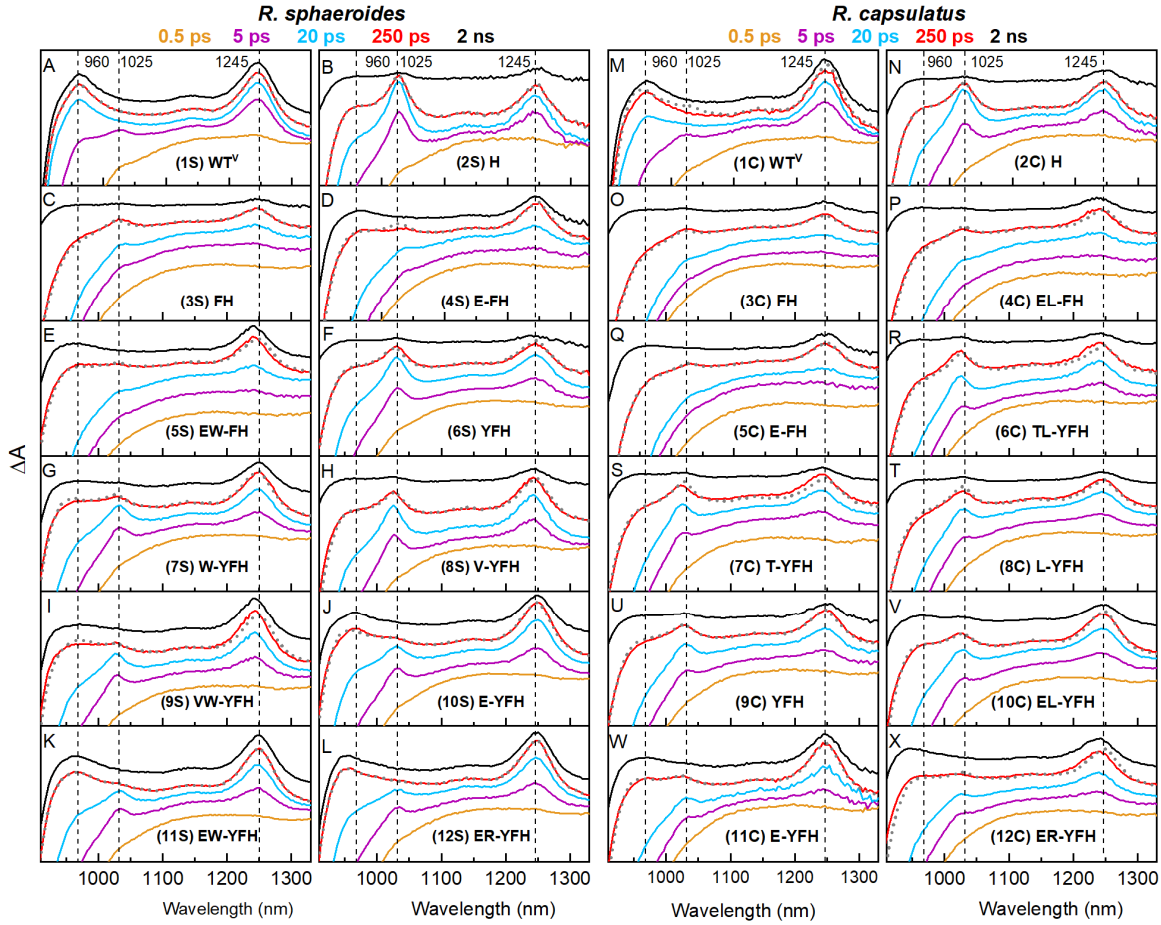

Figure 8. Representative NIR TA difference spectra for *R. sphaeroides* (left two panels) and *R. capsulatus* (right two panels) mutant RCs at 0.5 ps (gold), 5 ps (mauve), 20 ps (blue), 250 ps (red) and 2 ns (black). The vertical dashed lines indicate wavelengths for the H_B anion (960 nm; the peak is at shorter wavelength), BChl anions (1025 nm) and P^+ (1245 nm). The spectra are normalized to the same initial P* population. The gray dotted line overlapping the spectrum at 250 ps is a fit to basis spectra for $P^+H_B^-$, $P^+\beta_A^-$, and P*.

IV. DISCUSSION

4.1. Models and Mechanisms for Decay of P*.

Prior work has shown that fitting the P* stimulated-emission in WT *R. sphaeroides* and *R. capsulatus* RCs requires two exponentials with time constants (and relative amplitudes) of ~2–5 ps (~0.8–1) and ~8–12 ps (0.1–0.2), and various models have been applied to explain the observations [29,34,45-48,62-77]. Such models include pigment/protein relaxations, equilibria (involving P*, $P^+B_A^-$ and $P^+H_A^-$), "fast" and "slow" populations that both use two-step P* $\rightarrow$ $P^+B_A^-$ $\rightarrow$ $P^+H_A^-$ ET, and two populations with one using two-step ET and one using one-step P* $\rightarrow$ $P^+H_A^-$ superexchange ET. In various mutants exhibiting either only A-side ET [12,60,61,78-81] or both A- and B-side ET [10,27,56,59,82], minimally three exponentials are required to fit the P* decay. Suggested origins of this kinetic complexity include (1) multiple P* populations present at a given time after excitation and (2) a homogeneous system that evolves in time due to protein relaxations that could be rate limiting.

We recently described a hybrid approach [27] that draws on prior insights [83-89] that excitation of P to P* involves promotion of an electron from an antibonding to bonding MO. This will cause the two macrocycles of P to move closer together (and make it easier to oxidize). Upon oxidation, the distance will increase to an intermediate positon because the electron in the half-filled bonding orbital is removed. Such structural changes within P upon excitation (and oxidation) may elicit pigment/protein dynamics/relaxations and, in parallel or in series, generate multiple populations that will evolve with time. Motions that alter the relative disposition of the two macrocycles of P affect its properties, including the shorter (100–200 ps) P* internal-conversion time compared to that (~5 ns) for monomeric BChl* [85,90-95]. Thus, the properties of the "special pair" can impact the RC photochemistry across time scales [85].

For purpose of discussion, at a given time after excitation, P* populations in a sample differ in relative (1) free energies of the states and (2) contributions (and rate constants) of one- and two-step ET. The TA data and DADS for **11S** and **11C** (Figures 4–6) and the other mutants (Supplementary Information) support this view. The free energies of the states ($P^+B_B^-$, $P^+H_B^-$, P*, $P^+B_A^-$, $P^+\beta_A^-$) span ~200 meV or less in many mutants (Figures 2 and 3). The photodynamics involve (1) parallel ET to the A- and B-side cofactors, (2) one-and two-step ET on both branches, (3) thermal repopulation of one state from another, (4) some spectral changes that could be associated with B_B, B_A, or β_A, and (5) reversed energy ordering of two states in different P* populations. An example of the last point is that a population may exist in which $P^+H_B^-$ lies above $P^+B_B^-$ in free energy, with the latter decaying in part by charge recombination (*e.g.,* ~100–500 ps), in analogy to mutants in which a BPh (ϕ_B) replaces B_B [37,44,59]. Applying specific kinetic models and deriving rate constants for formation and decay routes for each state in the 24 mutants is beyond the scope of this paper. The overarching focus is the yield of $P^+H_B^-$, how this yield is impacted by mutations at specific sites near the cofactors and how the yield differs between *R. sphaeroides* and *R. capsulatus* analogs. Comparisons are facilitated by Figure 9, which shows bar graphs of the data in Table 2 and Figures 2 and 3.

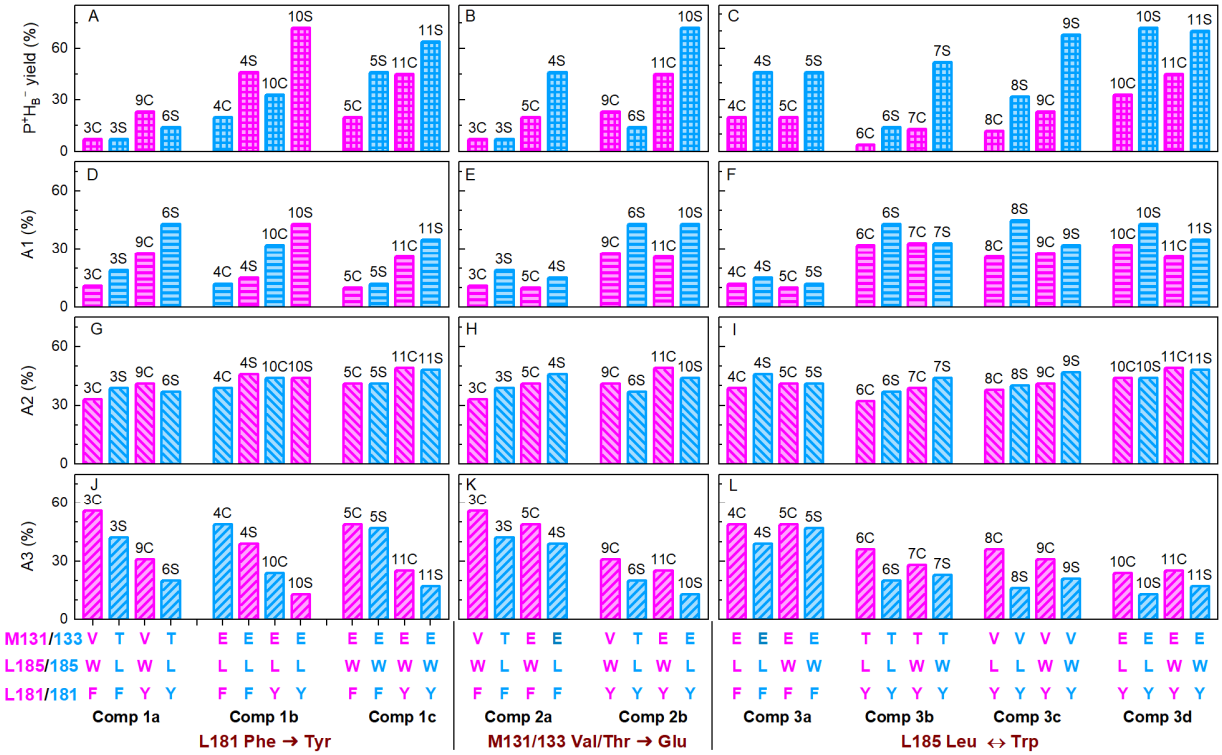

Figure 9. Comparisons of effects of mutations on the yield of $P^+H_B^-$ and amplitudes of ~4 ps (A1), ~20–50 ps (A2) and 100–200 ps (A3) P* decay components in *R. sphaeroides* mutant RCs (blue bars) and *R. capsulatus* mutants (magenta bars). These probed the effect of Tyr vs. native Phe at L181 (left column), Glu vs. native Val/Thr at M131/133 (middle column), and Trp vs. Leu at L185 (right column). Labels at top of bars refer to the *R. sphaeroides*(S)/*capsulatus*(C) mutant pair (Tables 1 and 2). See Figures 2 and 3 for further display of Comparisons 1a–3d.

4.2. Effect of Tyr vs. Phe at L181 Near H_B on Primary B-Side ET

Calculations suggest that $P^+B_A^-$ in WT RCs is stabilized by ~200 meV by the –OH dipole of TyrM210 [5-7]. About ~75% of this free-energy shift derives from making B_A easier to reduce and ~25% from making P easier to oxidize. In contrast, $P^+B_B^-$ is not similarly stabilized by symmetry-related PheL181 (near B_B and P) and lies above P* [6,7,36]. Stabilization of $P^+B_B^-$ provided by a Tyr at L181 triggers P* → $P^+B_B^-$ → $P^+H_B^-$ two-step ET and increases the yield of $P^+H_B^-$ regardless of the residues at M133/131 and L185. This is reflected in Figures 2, 3 and 9A in Comparison 1a (native residues at M133/131 and L185), Comparison 1b (Glu at M133/131 and

Leu at L185) and Comparison 1c (Glu at M133/131 and Trp at L185). In each case, the increase in $P^+H_B^-$ yield correlates with increased amplitude A_1 of the P_1* (~2–5 ps) kinetic component ("fast" population) (Figure 9D). Comparisons 1a–1c also reveal that amplitude A_2 of the P_2* (20–70 ps) population is relatively constant (Figure 9G) while the amplitude A_3 of the (slowest) P_3* population goes down (Figure 9J).

Because the F(L181)Y and Y(M210/208)F substitutions moderately (~25 mV) decrease and increase, respectively, the oxidation potential of P (Table 2) [6,62,63], they may alter the charge distribution in P*. However, prior work on heterodimer RCs in which one macrocycle or the other of P is changed from BChl to BPh has shown that the charge distribution in P is not the source of directionality of ET [32]. Thus, a change in the electronic structure of P is not expected to be the major source of the increase in $P^+H_B^-$ yield in the subset of mutants (Figures 2 and 3) wherein Phe is replaced by Tyr at L181 (**3S** → **6S**, **4S** → **10S**, **3C** → **9C**, **5C** → **11C**).

4.3. GluM133/M131 Provides Significant Yield of B-side ET with the Native Phe at L181

Stabilization of $P^+H_B^-$ by GluM133/131 near H_B increases the yield of $P^+H_B^-$. This is reflected in Figure 2 (M133Thr→Glu in *R. sphaeroides*), Figure 3 (M131Val→Glu in *R. capsulatus*) and Figure 9B (both species) via Comparison 2a (**3S** → **4S**, **3C** → **5C**; native Phe at L181 near B_B) and Comparison 2b (**6S** → **10S**, **9C** → **11C**; Tyr substituted at L181). In all cases, the increased $P^+H_B^-$ yield derives from increased amplitude A_2 of P_2* decay by "slow" (~20–70 ps) ET (Figure 9H). In parallel, there is a decrease in the relative amplitude A_3 of the P_3* (~150–250 ps) component (Figure 9K) and with little change or a small decrease in amplitude A_1 of the P_1* (~3–5 ps) two-step ET component (Figure 9E).

Most surprising in Comparison 2a is the substantial increase in the yield of $P^+H_B^-$ for *R. sphaeroides* **4S** (46%) vs. **3S** (7%) upon changing Thr to Glu at M133 near H_B with all the other native B-side residues retained, including PheL181. A smaller increase for *R. capsulatus* **5C** (20%) vs. **3C** (7%) is found upon changing Val to Glu at M131. Stabilization of $P^+H_B^-$ by GluM133/131 could increase the yield of $P^+H_B^-$ by improving the energy denominator for electronic mixing (superexchange). If a population exists that has $P^+H_B^-$ above P* to start with, stabilization of $P^+H_B^-$ by GluM133/131 could (1) move $P^+H_B^-$ below P* but above $P^+B_B^-$ (enabling superexchange ET) or (2) move $P^+H_B^-$ below $P^+B_B^-$ (enabling the second step in two-step ET).

4.4. Impact of Trp vs. Leu at L185 Near H_B on Primary B-Side ET

The YFH set of mutations (Table 1) in *R. capsulatus* (native Trp at L185) gives a higher yield of $P^+H_B^-$ than in *R. sphaeroides* (native Leu at 185) [10,18,21,22]. This finding is confirmed here (Figures 2 and 3); Figure 9C shows the higher yield of $P^+H_B^-$ in the YFH mutant RCs from *R. capsulatus* (23%; magenta bar **9C**) compared to *R. sphaeroides* (14%; blue bar **6S**). The *R. sphaeroides* W-YFH (**7S**) mutant RC substitutes Trp for Leu at L185. In Figure 9C, the ***$P^+H_B^-$ yield is more than 3-fold larger*** with TrpL185 (52%; blue bar **7S**) than native LeuL185 (14%; blue bar **6S**). In reverse, the *R. capsulatus* L-YFH (**8C**) mutant RC substitutes Leu for native Trp at L185 and the ***$P^+H_B^-$ yield is 2-fold lower*** with LeuL185 (12%; magenta bar **8C**) than TrpL185 (23%; magenta bar **9C**). The aromatic Trp is expected to stabilize nearby charge (*i.e.,* H_B^-), just as Trp residues facilitate hole/electron transfer in proteins [96,97].

A different set of comparisons couples variation of the residue at L185 (Trp or Leu) with that at M133/131 (Thr, Val or Glu) on the yield of $P^+H_B^-$, and affirms the utility of Trp.

The $P^+H_B^-$ yield with variation in M133 (native Thr) in *R. sphaeroides* is as follows:

• With LeuL185 (Figure 2 middle row): Thr (14%; **6S)** < Val (32%; **8S**) < Glu (72%; **10S**)

• With TrpL185 (Figure 2 bottom row): Thr (52%; **7S**) < Val (68%; **9S**) ~ Glu (70%; **11S**)

The $P^+H_B^-$ yield with variation at M131 (native Val) in *R. capsulatus* is as follows:

• With LeuL185 (Figure 3 bottom row): Thr (4%; **6C**) < Val (12%; **8C**) < Glu (33%; **10C**)

• With TrpL185 (Figure 3 middle row): Thr (13%; **7C**) < Val (23%; **9C**) < Glu (45%; **11C**)

The four comparisons show that Thr at M133/131 has the lowest $P^+H_B^-$ yield, followed by Val, followed by Glu with the highest yield. These results also show that whether M133/131 is Thr, Val or Glu, the $P^+H_B^-$ yield is higher when L185 is Trp vs. Leu. An exception is GluM133 in *R. sphaeroides* YFH where the yield is similar when L185 is Trp (**11S**) vs. Leu (**10S**). Perhaps in that case GluM133 stabilizes $P^+H_B^-$ sufficiently that the effect of Trp vs. Leu at L185 is marginal. The consistently lower yield of $P^+H_B^-$ with Thr vs. Val at M133/M131 may reflect a difference in size or that Thr can be a hydrogen bond donor or acceptor. Collectively, the results show that whether $P^+H_B^-$ is stabilized by TrpL185 or GluM133/M131, the increased $P^+H_B^-$ yield is attained by an increased contribution of the P_2* (20–70 ps) decay component (Figure 9I).

4.5. Effect of Arg at L185

R. sphaeroides/capsulatus pair 12 have Arg (rather than Leu/Trp) at L185 along with E-YFH. The $P^+H_B^-$ yields of 91% for **12S** and 53% for **12C** are the largest within both groups (Figures 2 and 3). We recently reported that the $P^+H_B^-$ yield for **12S** depends on the density of culture and associated pH (7.0–8.3) at the time of cell harvesting [27]. *R. sphaeroides* RCs from cultures grown to a lower density of cells (Klett ≤280 and pH ≤7.4) provide a high ~90% yield of $P^+H_B^-$, while RCs from cultures grown to a higher density of cells (Klett >280 and pH > 7.4)

provide a $P^+H_B^-$ yield of ~50–60%. We find here a $P^+H_B^-$ yield of ~50–60% regardless of Klett value for *R. capsulatus* **12C** RCs (Figure S11, Table S2).

The results on *R. capsulatus* **12C** are consistent with the linear correlation between $P^+H_B^-$ yield and the P* decay profile observed previously in *R. sphaeroides* **12S** [27]. In particular, Table 2 shows that the 91% yield of $P^+H_B^-$ for **12S** is attained via contributions of 40% P_1* (τ_1 = 4.0 ps), 50% P_2* (τ_2 = 22 ps) and 10% P_3* (τ_3 = 150 ps), whereas the 53% yield of $P^+H_B^-$ obtained for **12C** derives from 27% P_1* (τ_1 = 4.5 ps), 42% P_2* (τ_2 = 29 ps) and 31% P_3* (τ_3 = 156 ps). Thus, a higher $P^+H_B^-$ yield correlates with changes in the abundances of the three P* populations with a net result being an overall decrease in P_3* and increase in P_1*. The amount of the P_2* population is substantial across mutant pairs 4–12 (Table 2 and Figure 9).

4.6. Conclusions

This study probes sets of amino acids at three strategic locations in *R. sphaeroides* and *R. capsulatus* mutant RCs. The results provide insights into species differences and design principles as follows.

(1) A given *R. sphaeroides* RC has a consistently higher yield of $P^+H_B^-$ compared to the *R. capsulatus* analog. The yields range from ~5% to ~90% for *R. sphaeroides* and ~5% to ~60% for *R. capsulatus* (Table 2 and Figures 2, 3 and 9A).

(2) In concert with point 1, the contributions of P* $\rightarrow$ $P^+\beta_A^-$ A-side ET and P* $\rightarrow$ ground state are generally larger for *R. capsulatus* than *R. sphaeroides* RCs bearing identical amino acids at L185 and M133/131.

(3) In most cases, the amplitude A_1 of the P_1* rapid two-step ET component is greater for *R. sphaeroides* than *R. capsulatus* (Table 2 and Figure 9D–F).

(4) Target global analysis (Section S9) suggests that the first step in $P^* \rightarrow P^+B_B^- \rightarrow P^+H_B^-$ ET typically has time constant of ~3–4 ps and that the second step is two-fold or more slower. In comparison, the time constants for $P^* \rightarrow P^+B_A^- \rightarrow P^+H_A^-$ ET in WT RCs are ~3–4 ps and ~1 ps, respectively. Thus, although B-side two-step ET successfully delivers electrons to H_B in the mutants, this process is slower than occurs on the A side in native RCs.

(5) Slower (~20–70 ps) superexchange ET effectively directs electrons to the B side. For mutant pairs 4–12, ~30–50% of the $P^+H_B^-$ yield derives in this manner (Table 2 and Figure 9G–K).

(6) A relatively high (46%) yield of B-side ET to produce $P^+H_B^-$ is attained in the *R. sphaeroides* **4S** and **5S** RCs (vs. 7% for **3S**) that bear the native Phe at the linchpin site L181 in the FH background. The *R. capsulatus* RCs (**4C** and **5C**) show a parallel pattern vs. **3C** but with a smaller increase in yield (20% vs. 7%). In all four cases, the enabler is a single B-side mutation that places GluM133/131 near H_B.

The last two points support the view from prior studies of mutant **12S** [27,56] that rapid two-step ET is not a prerequisite for a high yield of unidirectional ET. The overall results also support the perspective that the ability to utilize both one-step and two-step initial ET in proportions depending on context adds robustness to the charge-separation process [29,30], as may protein dynamics that allow the RC to explore the configurational and energetic landscape [47,48].

Nine of twelve *R. sphaeroides* and *R. capsulatus* pairs explored herein have the same residue (Tyr or Phe) at L181 near P and B_B, the same residue (Glu, Thr, or Val) at M133/131 near H_B, and the same residue (Trp, Leu, or Arg) at L185 near H_B in the two species. For each such species pair, the *R. sphaeroides* RC has a consistently higher yield of $P^+H_B^-$ compared to the *R. capsulatus* analog. Such differences must derive from combined effects of residues at sites other than those probed here. Calculations indicate that the redox properties of the cofactors, and the free energies of the charge-separated states, are governed by both local cofactor-protein

interactions and global electrostatic effects of the protein, some involving residues distant from the cofactors [5-7,36]. It is difficult to predict off-hand those residues that could be responsible for the remaining species differences. These could be probed by additional saturation-mutagenesis studies, electrostatics calculations and molecular dynamics simulations, or artificial-intelligence (AI) methods. The results of the present study should aid or even guide such future efforts.

ACKNOWLEDGEMENTS

This work was supported by the U. S. Department of Energy, Office of Basic Energy Sciences under grant DE-CD0002036 (C.K. and D.H.) and associated Field Work Proposal (P.D.L.). Argonne, a U. S. Department of Energy Office of Science laboratory, is operated under Contract No. DE-AC02-06CH11357.

AUTHOR INFORMATION

Nikki Cecil M. Magdaong
Department of Chemistry
Washington University
St. Louis, MO 63130
Kaitlyn M. Faries
Department of Chemistry
Washington University
St. Louis, MO 63130

James C. Buhrmaster
Biosciences Division
Argonne National Laboratory
Lemont, IL 60439

Gregory A. Tira
Biosciences Division
Argonne National Laboratory
Lemont, IL 60439

Ryan M. Wyllie
Biosciences Division
Argonne National Laboratory
Lemont, IL 60439

Claire E. Kohout
Biosciences Division
Argonne National Laboratory
Lemont, IL 60439

Deborah K. Hanson
Biosciences Division
Argonne National Laboratory
Lemont, IL 60439

Philip D. Laible

Biosciences Division
Argonne National Laboratory
Lemont, IL 60439

Dewey Holten
Department of Chemistry
Washington University
St. Louis, MO 63130

Christine Kirmaier
Department of Chemistry
Washington University
St. Louis, MO 63130

Corresponding Author

*E-mail: kirmaier@wustl.edu. Tel: 314-935-6480

Declaration of interests: The authors declare that they have no known competing financial interests or personal relationships that could have appeared to influence the work reported in this paper.

REFERENCES

[1]. Deisenhofer, J.; Epp, O.; Miki, K.; Huber, R.; Michel, H. Structure of the Protein Subunits in the Photosynthetic Reaction Center from *Rhodopseudomonas viridis* at 3 Å Resolution. *Nature* **1985**, *318*, 618–624.

[2]. Allen, J. P.; Feher, G.; Yeates, T. O.; Komiya, H.; Rees, D. C. Structure of the Reaction Center from *Rhodobacter sphaeroides* R-26: The Cofactors. *Proc. Natl. Acad. Sci. U.S.A.* **1987**, *84*, 5730–5734.

[3]. Chang, C.-H.; El-Kabbani, O.; Tiede, D. M.; Norris, J. R.; Schiffer, M. The Structure of the Membrane-Bound Photosynthetic Reaction Center from *Rhodobacter sphaeroides* R-26. *Proc. Natl. Acad. Sci. U.S.A.* **1991**, *30*, 5352–5360.

[4]. Ermler,U.; Fritsch, G.; Buchanan, S. K.; Michel, H. Structure of the Photosynthetic Reaction Centre from *Rhodobacter sphaeroides* at 2.65 A Resolution: Cofactors and Protein-Cofactor Interactions. *Structure* **1994**, *2*, 925–936.

[5]. Alden, R. G.; Parson, W. W.; Chu, Z. T.; Warshel, A. Calculations of Electrostatic Energies in Photosynthetic Reaction Centers. *J. Am. Chem. Soc.* **1995**, *117*, 12284–12298.

[6]. Alden, R. G.; Parson, W. W.; Chu, Z. T.; Warshel, A. Orientation of the OH Dipole of Tyrosine (M)210 and Its Effect on Electrostatic Energies in Photosynthetic Bacterial Reaction Centers. *J. Phys. Chem.* **1996**, *100*, 16761–16770.

[7]. Gunner, M. R.; Nicholls, A.; Honig, B. Electrostatic Potentials in *Rhodopseudomonas viridis* Reaction Centers: Implications for the Driving Force and Directionality of Electron Transfer. *J. Phys. Chem.* **1996**, *100*, 4277–4291.

[8]. Heller, B. A.; Holten, D.; Kirmaier, C. Control of Electron Transfer to the L-Side Vs. the M-Side of the Photosynthetic Reaction Center. *Science* **1995**, *269*, 940–945.

[9]. Kirmaier, C.; Gaul, D.; DeBey, R.; Holten, D.; Schenck, C. C. Charge Separation in a Reaction Center Incorporating Bacteriochlorophyll in Place of Photoactive Bacteriopheophytin. *Science* **1991**, *251*, 922–927.

[10]. Magdaong, N.C.M.; Buhrmaster, J. C.; Faries, K. M.; Tira, G. A.; Lindsey, J. S.; Hanson, D. K.; Holten, D.; Laible, P. D.; Kirmaier, C. In Situ, Protein-Mediated Generation of a Photochemically Active

Chlorophyll Analog in a Mutant Bacterial Photosynthetic Reaction Center. *Biochemistry* **2021**, *60*, 1260–1275.

[11]. Kirmaier, C.; Laporte, L.; Schenck, C. C.; Holten, D. The Nature and Dynamics of the Charge-Separated Intermediate in Reaction Centers in Which Bacteriochlorophyll Replaces the Photoactive Bacteriopheophytin .2. The Rates and Yields of Charge Separation and Recombination. *J. Phys. Chem.* **1995**, *99*, 8910–8917.

[12]. Pan, J.; Saer, R.; Lin, S.; Beatty, J. T.; Woodbury, N. W. Electron Transfer in Bacterial Reaction Centers with the Photoactive Bacteriopheophytin Replaced by a Bacteriochlorophyll Through Coordinating Ligand Substitution. *Biochemistry* **2016**, *55*, 4909–4918.

[13]. Fajer, J.; Borg, D. C.; Forman, A.; Dolphin, D.; Felton, R. H. Anion Radical of Bacteriochlorophyll. *J. Am. Chem. Soc.* **1973**, *95*, 2739–2741.

[14]. Fajer, J.; Brune, D. C.; Davis, M. S.; Forman, A.; Spaulding, L. D. Primary Charge Separation in Bacterial Photosynthesis: Oxidized Chlorophylls and Reduced Pheophytin. *Proc. Natl. Acad. Sci. U.S.A.* **1975**, *72*, 4956–4960.

[15]. Coleman, W. J.; Bylina, E. J.; Youvan, D. C. Reconstitution of Photochemical Activity in *Rhodobacter Capsulatus* Reaction Centers Containing Mutation at Tryptophan M-250 in the Primary Quinone Binding Site. In *Current Research in Photosynthesis* (Baltscheffsky, M., Ed.) **1990**, pp 149–152, Kluwer, Dordrecht.

[16]. Wakeham, M. C.; Frolov, D.; Fyfe, P. K.; van Grondelle, R.; Jones, M. R. Acquisition of Photosynthetic Capacity by a Reaction Centre That Lacks the Q_a Ubiquinone; Possible Insights into the Evolution of Reaction Centres? *Biochim. Biophys. Acta* **2003**, *1607*, 53–63.

[17]. Weaver, J. B. Using Genetic Code Expansion to Investigate Electron Transfer Protein Electronstatics in the Photosynthethetic Reaction Center. Ph. D. Thesis; Stanford University, 2022, https://stacks.stanford.edu/file/druid:gv390gr2409/Dissertation_JaredWeaver_2022_06_02_Final-augmented.pdf

[18]. Dylla, N. P.; Faries, K. M.; Wyllie, R. M.; Swenson, A. M.; Hanson, D. K.; Holten, D.; Kirmaier, C.; Laible, P. D. Species Differences in Unlocking B-Side Electron Transfer in Bacterial Reaction Centers. *Febs. Lett.* **2016**, *590*, 2515–2526.

[19]. Cotton, T. M.; Van Duyne, R. P. An Electrochemical Investigation of the Redox Properties of Bacteriochlorophyll and Bacteriopheophytin in Aprotic Solvents. *J. Am. Chem. Soc.* **1979**, *101*, 7605–7612.

[20]. Allen, J. P.; Williams, J. C. Relationship Between the Oxidation Potential of the Bacteriochlorophyll Dimer and Electron Transfer in Photosynthetic Reaction Centers. *J Bioenerg Biomembr* **1995**, *27*, 275–283.

[21]. Kirmaier, C.; He, C; Holten, D. Manipulating the Direction of Electron Transfer in the Bacterial Reaction Center by Swapping Phe for Tyr Near $BChl_M$ (L181) and Tyr for Phe Near $BChl_L$ (M208). *Biochemistry* **2001**, *40*, 12132–12139.

[22]. Kirmaier, C.; Laible, P. D.; Hanson, D. K.; Holten, D. B-side Charge Separation in Bacterial Photosynthetic Reaction Centers: Nanosecond-Timescale Electron Transfer from H_B^- to Q_B. *Biochemistry* **2003**, *42*, 2016-2024.

[23]. Chuang, J. I.; Boxer, S. G.;Holten, D.; Kirmaier, C. Temperature Dependence of Electron Transfer to the M-Side Bacteriopheophytin in *Rhodobacter capsulatus* Reaction Centers. *J. Pys. Chem.* **2008**, *112*, 5487–5499.

[24]. Chuang, J. I.; Boxer, S. G.; Holten, D.; Kirmaier, C. High Yield of M-Side Electron Transfer in Mutants of *Rhodobacter Capsulatus* Reaction Centers Lacking the L-Side Bacteriopheophytin. *Biochemistry* **2006**, *45*, 3845–3851.

[25]. Robles, S. J.; Breton, J.; Youvan, D. C. Partial Symmetrization of the Photosynthetic Reaction Center, *Science* **1990**, *248*, 1402–1405.

[26]. Breton, J.; Martin, J. L.; Lambry, J. C.; Robles, S. J.; Youvan, D. C. Ground State and Femtosecond Transient Absorption Spectroscopy of a Mutant of *Rhodobacter capsulatus* Which Lacks the Initial Electron acceptor Bacteriopheophyrin, In *Structure and Function of Bacterial Photosynthetic Reaction Centers* (Michel-Beyerle, M. E., Ed.). **1990**, pp 293–302, Springer-Verlag, New York.

[27]. Laible, P. D.; Hanson, D. K.; Buhrmaster, J. C.; Tira, G. A.; Faries, K. M.; Holten, D.; Kirmaier, C. Switching Sides - Reengineered Primary Charge Separation in the Bacterial Photosynthetic Reaction Center. *Proc. Natl. Acad. Sci. U.S.A.* **2020**, *117*, 865–871.

[28]. Parson, W.W.; Chu, Z.-T.; Warshel, A. Electrostatic Control of Charge Separation in Bacterial Photosynthesis. *Biochim. Biophys. Acta* **1990**, *1017*, 251–272.

[29]. Bixon, M.; Jortner, J.; Michel-Beyerle, M. E. A Kinetic Analysis of the Primary Charge Separation in Bacterial Photosynthesis. Energy Gaps and Static Heterogeneity. *Chem. Phys.* **1995**, *197*, 389–404.

[30]. Bixon, M.; Jortner, J.; Michel-Beyerle, M. E. On the Mechanism of the Primary Charge Separation in Bacterial Photosynthesis. *Biochim. Biophys. Acta **1991**, 1056*, 301–315.

[31]. Wakeham, M.C.; Jones, M. R. Rewiring Photosynthesis: Engineering Wrong-Way Electron Transfer in Purple Photosynthetic Reaction Centre. *Biochemical Society Transactions*, **2005**, 33, 851–857.

[32]. Harris, M.A.; Luehr, C. A. ; Faries, K. M.; Wander, M.; Kressel, L.; Holten, D.; Hanson, D. K.; Laible, P. D.; C. Kirmaier C. Protein Influence on Charge-Asymmetry of the Primary Donor in Photosynthetic Bacterial Reaction Centers Containing a Heterodimer: Effects on Photophysical Properties and Electron Transfer. *J. Phys. Chem. B.* **2013**, *117*, 4028-4041.

[33]. Saggu, M. Carter, B.; Zhou, X.; Faries, K M.; Cegelski,L.; Holten, D.; Boxer, S. G.; Kirmaier, C. Putative Hydrogen Bond to Tyrosine M208 in Photosynthetic Reaction Centers from *Rhodobacter capsulatus* Significantly Slows Primary Charge Separation. *J. Phys. Chem. B* **2014**, *118*, 6721–6732.

[34]. Hartwich, G.; Lossau, H.; Michel-Beyerle, M. E.; Ogrodnik, A. Nonexponential Fluorescence Decay in Reaction Centers of *Rhodobacter Sphaeroides* Reflecting Dispersive Charge Separation up to 1 ns. *J. Phys. Chem. B* **1998**, *102*, 3815–3820.

[35]. Schmidt, S.; Arlt, T.; Hamm, P; Huber, H.; Nagele,T.; Wachtveitl, J.; Meyer, H.; Scheer, H.; Zinth, W. Energetics of the Primary Electron Transfer Reaction Revealed by Ultrafast Spectroscopy on Modified Bacterial Reaction Centers. *Chem. Phys. Lett.* **1994**, *223*, 116–120 (1994).

[36]. Warshel, a.; Chu, Z, T,; Parson, W. W. On the Energetics of the Primary Electron-Transfer Process in Bacterial Reaction Centers. *J. Photochem. Photobiol. A-Chem.* **1994**, *82*, 123–128 (1994).

[37]. Katilius, E.; Babendure, J. L.; Katiliene, Z.; Lin, S.; Taguchi, A. K. W.; Woodbury, N. W. Manipulations of the B-Side Charge-Separated States' Energetics in the *Rhodobacter sphaeroides* Reaction Center. *J. Phys. Chem. B* **2003**, *107*, 12029–12034.

[38]. Volk, M.; Aumeier, G.; Langenbacher, T.; Feick, R.; Ogrodnik, A. Michel-Beyerle, M. E. Energetics and Mechanism of Primary Charge Separation in Bacterial Photosynthesis. A Comparative Study on Reaction Centers of *Rhodobacter sphaeroides* and *Chloroflexus aurantiacus*. *J. Phys. Chem. B* **1998**, *102*, 735-751.

[39]. Gunner, M. The Reaction Center Protein from Purple Bacteria: Structure and Function. *Current Topics in Bioenergetics* **1991**, *16*, 319-367.

[40]. Goldstein, R. A. Boxer, S. G. The Effect of Very High Magnetic Fields on the Reaction Dynamics in Bacterial Reaction Centers: Implication for the Reaction Mechanism. *Biochim. Biophys. Acta* **1989**, *977*, 78-86.

[41]. Ogrodnik, a.; Volk, M.; Letterer, R. Feick, R.; Michel-Beyerle, M. E. Determination of Free Energies in Reaction Centers of Rb. Sphaeroides. *Biochim. Biophys. Acta.* **1988**, *936*, 361–371.

[42] Woodbury, N. W.; Parson, W. W. Nanosecond Fluorescence From Isolated Photosynthetic Reaction Centers of Rhodopseudomonas Sphaeroides. *Biochim. Biophys. Acta* **1984**, *767*, 345–361.

[43]. Katilius, E.; Katiliene, Z.; Lin, S.; Taguchi, A. K. W.; Woodbury, N. W. B-side Electron Transfer in the HE(M182) Reaction Center Mutant from *Rhodobacter sphaeroides*. *J. Phys. Chem. B* **2002**, *106*, 12344–12350.

[44]. Katilius, E.; Turanchik, T.; Lin, S.; Taguchi, A. K. W.; Woodbury, N. W. B-Side Electron Transfer in a Rhodobacter sphaeroides Reaction Center Mutant in Which the B-Side Monomer Bacteriochlorophyll is Replaced with Bacteriopheophytin . *J. Phys. Chem. B* **1999**, *103*, 7386–7389.

[45] Peloquin, J,M.; Williams, J. C.; Lin, X.; Alden, R. G.; Taguchi, A. K. W.; Allen, J. P.; Woodbury, N. W. Time-Dependent Thermodynamics During Early Electron Transfer in Reaction Centers from Rhodobacter sphaeroides *Biochemistry* **1994**, *33*, 8089–8100.

[46]. N. W. Woodbury, J. M. Peloquin, R. G. Alden, X. Lin, S. Lin, A. K. W. Taguchi, J. C. Williams, J. P. Allen, Relationship between Thermodynamics and Mechanism during Photoinduced Charge Separation in Reaction Centers from *Rhodobacter Sphaeroides*. *Biochemistry* **33**, 8101-8112 (1994).

[47]. Wang, H. Y.; Lin, S.; Allen, J. P.; Williams, J. C.; Blankert, S.; Laser, C.; Woodbury, N. W. Protein Dynamics Control the Kinetics of Initial Electron Transfer in Photosynthesis. *Science* **2007**, *316*, 747–750.

[48] Wang, H. Y.; Hao, Y., Jiang, Y., Lin, S.; Woodbury, N. W. Role of Protein Dynamics in Guiding Electron-Transfer Pathways in Reaction Centers from Rhodobacter sphaeroides. *J. Phys. Chem. B* **2007**, *116*, 711–717.

[49]. K. Gibasiewicz, M. Pajzderska, A. Dobek, J. Karolczak, G. Burdzinski, K. Brettel, M. R. Jones, Analysis of the temperature-dependence of $P^+H_A^-$ charge recombination in the *Rhodobacter sphaeroides* reaction center suggests nanosecond temperature-independent protein relaxation. *Phys Chem Chem Phys* **15**, 16321-16333 (2013).

[50]. K. Dubas, M. Baranowski, A. Podhorodecki, M. R. Jones, K. Gibasiewicz, Unified Model of Nanosecond Charge Recombination in Closed Reaction Centers from Rhodobacter sphaeroides: Role of Protein Polarization Dynamics. *J. Phys. Chem. B* **120**, 4890-4896 (2016).

[51]. Bylina, E. J.; Kirmaier, C.; McDowell, L. M.; Holten, D.; Youvan, D. C. Influence of an Amino Acid Residue on the Optical Properties and Electron Transfer Dynamics of a Photosynthetic Reaction Center Complex. *Nature* **1988**, *336*, 182–184.

[52]. Kirmaier, C.; Laporte, L.; Schenck, C. C.; Holten, D. The Nature and Dynamics of the Intermediate State P^+I^- in Reaction Centers in which the Photoactive Bacteriopheophytin is Replaced by Bacteriochlorophyll. II. The Rates and Yields of Electron Transfer and Charge Recombination. *J. Phys. Chem.* **1995**, *99*, 8910-8917.

[53]. Nabedryk, E.; Allen, J. P.; Taguchi, A. K. W.; Williams, J. C.; Woodbury, N. W.; Breton, J. Fourier-Transform Infrared Study of the Primary Electron-Donor in Chromatophores of *Rhodobacter Sphaeroides* with Reaction Centers Genetically-Modified at Residue-M160 and Residue-L131. *Biochemistry* **1993**, *32*, 13879–13885.

[54]. Kirmaier, C.; Cua, A.; He, C.; Holten, D.; Bocian, D. F. Probing M-Branch Electron Transfer and Cofactor Environment in the Bacterial Photosynthetic Reaction Center by the Addition of a Hydrogen Bond to the M-side Bacteriopheophytin. *J. Phys. Chem. B* **2002**, *106*, 495–503.

[55]. Kressel, L.; Faries, K. M.; Wander, M. J.; Zogzas, C. E.; Mejdrich, R. J.; Hanson, D. K.; Holten, D.; Laible, P. D.; Kirmaier, C. High Yield of Secondary B-Side Electron Transfer in Mutant Rhodobacter Capsulatus Reaction Centers. *Biochim. Biophys. Acta* **2014**, *1837*, 1892–1903.

[56]. Magdaong, M. C.M.; Faries, K. M.; Buhrmaster, J. C.; Tira, G. A.; Wyllie, R. M.; Kohout, C. E.; Hanson, D. K.; Laible, P. D.; Holten, D.; Kirmaier, C. High Yield of B-side Electron Transfer at 77 K in the Photosynthetic Reaction Center Protein from Rhodobacter Sphaeroides, *J. Phys. Chem. B* **2022**, *126*, 8940–8956.

[57]. K. M. Faries, L. L. Kressel, M. J. Wander, D. Holten, P. D. Laible, C. Kirmaier, and D. K. Hanson, High-Throughput Engineering to Revitalize a Vestigial Electron Transfer Pathway in Bacterial Photosynthetic Reaction Centers. *J. Biol. Chem.* **2012**, *287*, 8507–8514.
[58]. Sistrom, W. R. Transfer of chromosomal genes mediated by plasmid R68.45 in *Rhodopseudomonas sphaeroides*. J. Bact. **1977**, *131*, 526-532.
[59]. Faries, K. M.; Dylla, N. P.; Hanson, D. K.; Holten, D.; Laible, P. D.; Kirmaier, C. Manipulating the Energetics and Rates of Electron Transfer in *Rhodobacter Capsulatus* Reaction Centers with Asymmetric Pigment Content. *J. Phys. Chem. B* **2017**, *121*, 6989–7004.
[60]. Wang, H. Y.; Lin, S.; Katilius, E.; Laser, C.; Allen, J. P.; Williams, J. C.; Woodbury, N. W. Unusual Temperature Dependence of Photosynthetic Electron Transfer due to Protein Dynamics. *J. Phys. Chem.* **2009**, *113*, 818–824.
[61]. J. Pan, R. G. Saer, S. Lin, Z. Guo, J. T. Beatty, N. W. Woodbury, The Protein Environment of the Bacteriopheophytin Anion Modulates Charge Separation and Charge Recombination in Bacterial Reaction Centers. *J. Phys. Chem. B* **117**, 7179-7189 (2013).
[62]. Nagarajan, V.; Parson, W. W.; Davis, D.; Schenck, C. C. Kinetics and Free Energy Gaps of Electron Transfer Reactions in *Rhodobacter Sphaeroides* Reaction Centers. *Biochemistry* **1993**, *32*, 12324–12336.
[63]. Jia, Y.; DiMagno, T. J.; Chan, C.-K.; Wang, Z.; Du, M.; Hanson, D. K.; Schiffer, M.; Norris, J. R.; Fleming, G. R.; Popov, M. S. Primary Charge Separation in Mutant Reaction Centers of *Rhodobacter capsulatus*. *J. Phys. Chem.* **1993**, *97*, 13180–13191.
[64]. Zinth, W.; Wachtveitl, J. The first picoseconds in bacterial photosynthesis - Ultrafast electron transfer for the efficient conversion of light energy. *Chemphyschem* **2005**, *6*, 871–880.
[65]. Kirmaier, C.; Holten, D. Evidence That a Distribution of Bacterial Reaction Centers Underlies the Temperature- and Detection-Wavelength-Dependence of the Rates of the Primary Electron Transfer Reactions. *Proc. Natl. Acad. Sci. U.S.A.* **1990**, *97*, 3522–3556.
[66]. Vos, M. H.; Lambry, J. C.; Robles, S. J.; Youvan, D. C.; Breton, J.; Martin, J. L. Direct Observation of Vibrational Coherence in Bacterial Reaction Centers Using Femtosecond Absorption Spectroscopy. *Proc. Natl. Acad. Sci. U.S.A.* **1991**, *88*, 8885–8889.
[67]. Du, M.; Rosenthal, S. J.; Xie, X.; DiMagno, T. J.; Schmidt, M.; Hanson, D. K.; Schiffer, M.; Norris, J. R.; Fleming, G. R. Femtosecond Spontaneous-Emission Studies of Reaction Centers from Photosynthetic Bacteria. *Proc. Natl. Acad. Sci. U.S.A.* **1992**, *89*, 8517–8521.
[68]. Müller, M. G.; Griebenow, K.; Holzarth, A. R. Primary Processes in Isolated Bacterial Reaction Centers from *Rhodobacter Sphaeroides* Studied by Picosecond Fluorescence Kinetics. *Chem. Phys. Lett.* **1992**, *199*, 465–469.
[69]. Hamm, P.; Gray, K. A.; Oesterhelt, D.; Feick, R.; Scheer, H.; Zinth, W. Subpicosecond Emission Studies of Bacterial Reaction Centers. *Biochim. Biophys. Acta* **1993**, *1142*, 99–105.
[70]. Peloquin, J. M.; Lin, S.; Taguchi, A. K. W.; Woodbury, N. W. Excitation Wavelength Dependence of Bacterial Reaction Center Photochemistry. 2. Low-Temperature Measurements and Spectroscopy of Charge Separation. *J. Phys. Chem.* **1996**, *100*, 1428–14235.
[71]. Holzwarth, A. R.; Müller, M. G. Energetics and Kinetics of Radical Pairs in Reaction Centers from *Rhodobacter Sphaeroides*. A Femtosecond Transient Absorption Study *Biochemistry* **1996**, *35*, 11802–11831.
[72]. Beekman, L. M. P.; vanStokkum, I. H. M.; Monshouwer, R.; Rijnders, A. J.; McGlynn, P.; Visschers, R. W.; Jones, M. R.; vanGrondelle, R. Primary Electron Transfer in Membrane-Bound Reaction Centers with Mutations at the M210 Position. *J. Phys. Chem.* **1996**, *100*, 7256–7268.
[73]. Laible, P. D.; Greenfield, S. R.; Wasielewski, M. R.; Hanson, D. K.; Pearlstein, R. M. Antenna Excited State Decay Kinetics Establish Primary Electron Transfer in Reaction Centers as Heterogeneous. *Biochemistry* **1997**, *36*, 8677–8685.

[74]. Yakovlev, A. G.; Shkuropatov, A. Y.; Shuvalov, V. A. Nuclear Wavepacket Motion between P* and $P^+B_A^-$ Potential Surfaces with Subsequent Electron Transfer to H_A in Bacterial Reaction Centers. 1. Room Temperature. *Biochemistry* **2002**, *41*, 2667–2674.
[75]. Kakitani, T. Hou, A.; Miyasako, Y.; Koyama, K.; Nagae, H. Rates of the initial two steps of electron transfer in reaction centers from *Rhodobacter sphaeroides* as determined by singular-value decomposition followed by global fitting. *Chem. Phys. Lett.***2010**, *492*, 142–149.
[76]. Zhu, J. Y. ; van Stokkum, I. H. M.; Paparelli, L. Jones, M. R.; Groot, M. L. Early Bacteriopheophytin Reduction in Charge Separation in Reaction Centers of Rhodobacter sphaeroides. *Biophys J* **2013**, *104*, 2493–2502.
[77]. Weaver, J. B.; Lin, C-Y. Faries, K. M.; Mathews, I. I.; Russi, S.; Holten, D.; Kirmaier, C.; Boxer. S. G. Photosynthetic Reaction Center Variants Made via Genetic Code Expansion Show Tyr at M210 Tunes the Initial Electron Transfer Mechanism, *Proc. Nat. Acad. Sci. U.S.A.* **2021**, *118*, e2116439118.
[78]. Kundu, P. Application of Dyanmic Disorder Approach to the Temperature Dependent Non-exponential Electron Transfer Kinetics in Rhodopseudomonas Viridis. *J. Stat. Mech.* **2019**, 093501.
[79]. Kundu, P. Kinetics of Initial Charge Separation in the Photosynthetic Reaction Centers of *Rhodobacter sphaeroides*. *J. Phys. Chem. B* **2022**, *126*, 3470–3476.
[80]. LeBard, D. N., and Matyushov, D. V. (2008) Energetics and Kinetics of Bacterial Photosynthesis. J. Phys. Chem. B 112, 10322−10342.
[81]. LeBard, D. N., and Matyushov, D. V. (2009) Energetics of Bacterial Photosynthesis. J. Phys. Chem. B 113, 12424−12437.
[82]. Kirmaier, C.; Laible, P. D.; Hinden, E.; Hanson, D. K.; Holten, D. Detergent Effects on Primary Charge Separation in Wild-Type and Mutant *Rhodobacter Capsulatus* Reaction Centers. *Chem. Phys.* **2003**, *294*, 305–318.
[83]. Donohoe, R. J.; Duchowski, J. K.; Bocian, D. F. Hole delocalization in oxidized cerium(IV) porphyrin sandwich complexes. *J. Am. Chem. Soc.* **1988**, *110*, 6119–6124.
[84]. O. Bilsel, O.; Rodriguez, J; Milam, S. N.; Gorlin, P. A.; Girolami, G. S.; Suslick, K. S.; Holten, D. Electronic States and Optical-Properties of Porphyrins in Vanderwaals Contact - Th(Iv) Sandwich Complexes. *J. Am. Chem. Soc.* **1992**, *114*, 6528–6538.
[85]. Warshel A. Role of the Chlorophyll Dimer in Bacterial Photosynthesis. *Proc. Natl. Acad. Sci. U.S.A.* **1980**, *77*, 3105–3109.
[86]. Thompson, M. A.; Zerner, M.; Fajer, J, A Theoretical-Examination of the Electronic-Structure and Excited-States of the Bacteriochlorophyll B Dimer from Rhodopseudomonas-Viridis. *J. Phys. Chem.* **1991**, *95*, 5693–5700.
[87]. Scherer, P. O. J. ; Fischer, S. F. Quantum Treatment of the Optical Spectra and the Initial Electron Transfer Process within the Reaction Center of *Rhodopseudomonas Viridis*. *Chem. Phys.* **1989**, *131*, 115–127.
[88]. Breton, J.; Naberdryk, E,; Parson, W. W., A New Infrared Electronic Transition of the Oxidized Primary Electron Donor in Bacterial Reaction Centers: A Way to Assess Resonance Interactions between the Bacteriochlorophylls, Biochemistry 1992, 31, 7503–7510.
[89]. Warshel, A., & Parson, W. W. Spectroscopic Properties of Photosynthetic Reaction Centers. 1. Theory. J. Am. Chem. Soc. 1987, 109, 6143-6152.
[90]. M. H. Vos, J. C. Lambry, S. J. Robles, D. C. Youvan, J. Breton, J. L. Martin, Direct observation of vibrational coherence in bacterial reaction centers using femtosecond absorption spectroscopy. *Proc. Natl. Acad. Sci. U.S.A.* **88**, 8885-8889 (1991).
[91]. V. Tiwari, W. K. Peters, D. M. Jonas, Electronic resonance with anticorrelated pigment vibrations drives photosynthetic energy transfer outside the adiabatic framework. *Proc. Natl. Acad. Sci. U.S.A.* **110**, 1203-1208 (2013).

[92]. T. R. Middendorf, L. T. Mazzola, D. F. Gaul, C. C. Schenck, S. G. Boxer, Photochemical Hole-Burning Spectroscopy of a Photosynthetic Reaction Center Mutant with Altered Charge Separation Kinetics - Properties and Decay of the Initially Excited-State. *J. Phys. Chem.* **95**, 10142-10151 (1991).
[93]. K. Czarnecki, J. R. Diers, V. Chynwat, J. P. Erickson, H. A. Frank, D. F. Bocian, Characterization of the strongly coupled, low-frequency vibrational modes of the special pair of photosynthetic reaction centers via isotopic labeling of the cofactors. *J. Am. Chem. Soc.* **119**, 415-426 (1997).
[94]. S. G. Johnson, D. Tang, R. Jankowiak, J. M. Hayes, G. J. Small, D. M. Tiede, Primary Donor State Mode Structure and Energy-Transfer in Bacterial Reaction Centers. *J. Phys. Chem.* **94**, 5849-5855 (1990).
[95]. L. M. McDowell, D. Gaul, C. Kirmaier, D. Holten, C. C. Schenck, Investigation into the Source of Electron Transfer Asymmetery in Bacterial Reaction Centers. *Biochemistry* **30**, 8315-8322 (1991).
[96]. Wittekindt, C.; Schwarz, M.; Friedrich, T.; Koslowski, T. Aromatic Amino Acids as Stepping Stones in Charge Transfer in Respiratory Complex I: An Unusual Mechanism Deduced from Atomistic Theory and Bioinformatics. *J. Am. Chem. Soc.* **2009**, *131*, 8134–8140.
[97]. Gray, H. B.; Winkler, J. R. Hole Hopping Through Tyrosine/Tryptophan Chains Protects Proteins from Oxidative Damage. *Proc. Nat. Acad. Sci. U.S.A.* **2015**, *112*, 10920–10925.